

1 **TITLE**

2 **Systematic mapping of genetic interactions for *de novo* fatty acid synthesis**

3

4 **AUTHORS**

5 Michael Aregger^{1,*}, Keith A. Lawson^{1,2,3,*}, Maximillian Billmann^{4,*}, Michael Costanzo¹,
6 Amy H. Y. Tong¹, Katherine Chan¹, Mahfuzur Rahman⁴, Kevin R. Brown¹, Catherine
7 Ross¹, Matej Usaj¹, Lucy Nedyalkova¹, Olga Sizova¹, Andrea Habsid¹, Judy Pawlings⁵,
8 Zhen-Yuan Lin⁵, Hala Abdounis⁵, Alexander Weiss¹, Patricia Mero¹, James W. Dennis⁵,
9 Anne-Claude Gingras^{2,5}, Chad L. Myers^{4,6,#}, Brenda J. Andrews^{1,2,#}, Charles Boone^{1,2,#}, &
10 Jason Moffat^{1,2,7#}

11

12 *Authors contributed equally

13 #Corresponding authors

14

15 ¹Donnelly Centre, University of Toronto, 160 College Street, Toronto, Ontario, M5S 3E1,
16 Canada

17 ²Department of Molecular Genetics, University of Toronto, 160 College Street, Toronto,
18 Ontario, M5S 3E1, Canada

19 ³Division of Urology, Department of Surgery, University of Toronto

20 ⁴Department of Computer Science and Engineering, University of Minnesota – Twin Cities,
21 200 Union Street, Minneapolis, MN, 55455, USA

22 ⁵Lunenfeld-Tanenbaum Research Institute, Mount Sinai Hospital, Toronto, Ontario, M5G
23 1X5, Canada

24 ⁶Bioinformatics and Computational Biology Graduate Program, University of Minnesota –
25 Twin Cities, 200 Union Street, Minneapolis, MN, 55455, USA

26 ⁷Institute for Biomaterials and Biomedical Engineering, 160 College Street, Toronto,
27 Ontario, M5S 3E1, Canada

28 **ABSTRACT**

29 The *de novo* synthesis of fatty acids has emerged as a therapeutic target for various
30 diseases including cancer. While several translational efforts have focused on direct
31 perturbation of *de novo* fatty acid synthesis, only modest responses have been associated
32 with mono-therapies. Since cancer cells are intrinsically buffered to combat metabolic
33 stress, cells may adapt to loss of *de novo* fatty acid biosynthesis. To explore cellular
34 response to defects in fatty acid synthesis, we used pooled genome-wide CRISPR
35 screens to systematically map genetic interactions (GIs) in human HAP1 cells carrying a
36 loss-of-function mutation in *FASN*, which catalyzes the formation of long-chain fatty acids.
37 *FASN* mutant cells showed a strong dependence on lipid uptake that was reflected by
38 negative GIs with genes involved in the LDL receptor pathway, vesicle trafficking, and
39 protein glycosylation. Further support for these functional relationships was derived from
40 additional GI screens in query cell lines deficient for other genes involved in lipid
41 metabolism, including *LDLR*, *SREBF1*, *SREBF2*, *ACACA*. Our GI profiles identified a
42 potential role for a previously uncharacterized gene *LUR1 (C12orf49)* in exogenous lipid
43 uptake regulation. Overall, our data highlights the genetic determinants underlying the
44 cellular adaptation associated with loss of *de novo* fatty acid synthesis and demonstrate
45 the power of systematic GI mapping for uncovering metabolic buffering mechanisms in
46 human cells.

47 INTRODUCTION

48 Lipid metabolism as a source of energy for cancer cells, supporting rapid cell division and
49 contributing to cell survival, and fatty acid derivatives play key roles in oncogenic
50 signalling. Alterations in lipid metabolism, specifically the uptake of lipids and/or synthesis
51 of fatty acids, comprise different aspects of metabolic reprogramming that are well
52 documented in cancer and other indications, including metabolic syndrome and fatty liver
53 disease (Chen & Huang, 2019). *De novo* fatty acid synthesis has gained significant
54 traction as a targetable pathway following observations that overexpression of *FASN*,
55 which encodes fatty acid synthase and catalyzes the formation of long chain fatty acids,
56 and *ACACA*, which codes for Acetyl-CoA Carboxylase Alpha and acts directly upstream
57 of *FASN*, are associated with decreased survival rates for numerous solid malignancies
58 (Chen *et al*, 2019; Imoto, 2018; Menendez & Lupu, 2017; Garber, 2016; Röhrig & Schulze,
59 2016). Efforts to develop and translate small molecule inhibitors of *FASN* (e.g. TVB-2640)
60 have helped validate this enzyme as a targetable liability in cancer (Jones & Infante, 2015;
61 Benjamin *et al*, 2015), and have led to several clinical trials (e.g. *NCT02223247*,
62 *NCT02948569*, *NCT03179904*, *NCT02980029*). Given that metabolic pathways are highly
63 buffered to deal with environmental change, genetic screening approaches are a powerful
64 strategy to reveal metabolic regulatory mechanisms that underscore metabolic
65 redundancy, cross-talk and plasticity (Birsoy *et al*, 2014, 2015). An understanding of how
66 cells adapt to perturbation of *de novo* fatty acid synthesis could help identify new
67 targetable vulnerabilities that may inform novel therapeutic strategies or biomarker
68 approaches.

69

70 Mapping genetic interaction (GI) networks provides a powerful approach for identifying the
71 functional relationships between genes and their corresponding pathways. The systematic
72 exploration of pairwise GIs in model organisms revealed that GIs often occur among

73 functionally related genes and that GI profiles organize a hierarchy of functional modules
74 (Costanzo *et al*, 2016; Fischer *et al*, 2015). Thus, GI mapping has become an effective
75 strategy for identifying functional modules and annotating the roles of previously
76 uncharacterized genes. Model organism GI mapping has also provided insight into the
77 mechanistic basis of cellular plasticity or phenotypic switching that occurs as cells evolve
78 within their environments (Harrison *et al*, 2007; Szappanos *et al*, 2011). Accordingly, the
79 insights gained through systematic interrogation of GIs have fuelled significant interest to
80 leverage these approaches towards functionally annotating the human genome.

81

82 Recent technological advances using CRISPR-Cas enable the systematic mapping of GIs
83 in human cells (Wright *et al*, 2016; Doench, 2018). Here, we explore genome-wide GI
84 screens within the context of human query mutant cells defective for *de novo* fatty acid
85 synthesis. We systematically mapped genome-wide GI profiles for six genes involved in
86 lipid metabolism, revealing cellular processes that pinpoint genetic vulnerabilities
87 associated with defects in *de novo* fatty acid synthesis. In particular, negative GIs with
88 known fatty acid synthesis genes tend to identify other genes that are associated with this
89 process, including a previously uncharacterized gene *C12orf49* (*LUR1*), which appears to
90 function as a regulator of exogenous lipid uptake. Collectively, our data support the
91 strategy of systematically mapping digenic interactions using knockout query cell lines for
92 identifying buffering mechanisms within metabolism.

93 RESULTS

94 Systematic identification of genetic interactions for *de novo* fatty acid synthesis

95 *De novo* fatty acid synthesis is a multi-step enzymatic process that converts cytosolic
96 acetyl-CoA, malonyl-CoA, and NADPH to palmitate. Palmitate can be used directly or
97 further elongated and/or undergo desaturation to form alternate lipid species. To
98 systematically identify GIs associated with this metabolic process, we performed genome-
99 wide CRISPR screens in coisogenic cell lines either wild-type or deficient in FASN, a *de*
100 *novo* fatty acid synthesis enzyme that is frequently overexpressed in malignancies (Röhrig
101 & Schulze, 2016; Currie *et al*, 2013) (**Figure 1a**). We chose the human near-haploid cell
102 line HAP1 as a model system, given the relative ease for generating knockout (KO)
103 mutations in this background (Carette *et al*, 2011). We first validated our clonal FASN-KO
104 cells by confirming loss of FASN protein levels by western blot (**Figure S1a**). We also
105 performed targeted metabolite profiling of our parental HAP1 and FASN-KO cells, which
106 revealed a significant increase in the FASN substrate malonyl-CoA in the FASN-KO cells,
107 demonstrating their suitability as a model system for defective *de novo* fatty acid synthesis
108 (**Figure S1b**).

109

110 To map FASN GIs, we performed genome-wide CRISPR screens using the sequence
111 optimized TKOv3 gRNA library (Hart *et al*, 2017) in both the FASN-KO query cell line and
112 control wild-type (WT) HAP1 cells, and we compared the relative abundance of individual
113 gRNAs between the screen start (T0) and end (T18) time points (**Figure 1a-b**). The
114 relative abundance of gRNAs targeting each of ~18,000 genes in WT cells provides an
115 estimate of single mutant fitness, whereas the relative abundance of gRNAs in a query
116 mutant cell line provides an estimate of double mutant fitness. Since mutant phenotypes
117 can strongly depend on culture conditions (Billmann *et al*, 2018) and most standard cell
118 culture media contains supra-physiological nutrient levels that could mask phenotypic

119 effects of perturbing certain metabolic pathways, we performed our screens utilizing media
120 conditions containing the minimum amounts of glucose and glutamine required to sustain
121 proliferation of HAP1 cells; termed limiting media (**Figure S1c**, see Methods).

122

123 We developed a quantitative genetic interaction (qGI) score that measures the strength
124 and significance of genetic interactions by comparing the relative abundance of gRNAs in
125 a given query mutant cell line to the relative abundance of gRNAs targeting the
126 corresponding genes in an extensive panel of 21 genome-wide WT HAP1 screens (**Figure**
127 **1b**, see Methods). In this context, negative interactions are identified as genes whose
128 corresponding gRNAs exhibit significantly decreased abundance in a mutant KO
129 background relative to the control WT HAP1 cell line, whereas positive interactions reflect
130 genes with increased gRNA abundance in a mutant cell line relative to the parental line.

131

132 We performed three independent genome-wide, GI screens using our *FASN*-KO query
133 mutant cell line. Because GIs rely on accurate measurement of single and double mutant
134 phenotypes, we first examined the reproducibility of our single and double mutant fitness
135 measurements (see Methods). We observed a strong agreement of single gene fitness
136 effects (LFC) among 21 replicate WT HAP1 ($r > 0.87$) (**Figure S1d**) and double mutant
137 fitness effects derived from independent *FASN*-KO replicate screens ($r > 0.89$) (**Figure**
138 **1c**). Moreover, all three *FASN* screens robustly discriminated a set of reference essential
139 genes from non-essential genes (**Figures S1e-f**).

140

141 The identification of qGI scores depends on comparison of single mutant fitness
142 measurements in a WT HAP1 cell screen and double mutant fitness measurements in a
143 query mutant screen, both of which have inherent variability associated with them;
144 therefore, the reproducibility of qGIs is expected to be more challenging than the

145 measurement of either single or double mutant fitness phenotypes. Indeed, modest
146 agreement was observed between qGI scores of the three *FASN*-KO replicate screens
147 prior to filtering for significant interactions (pairwise $r = 0.29$ to 0.44) (**Figure 1d**). The
148 pairwise correlation between replicate screens increased substantially when we
149 considered GIs found to be significant ($|qGI| > 0.5$, $FDR < 0.5$) in at least one ($r = 0.52$ -
150 0.69) or two ($r = 0.86$ - 0.94) *FASN*-KO replicate screens (**Figure 1d, Table S1**).

151

152 Leveraging all 3 *FASN*-KO replicates, we developed a reproducibility score that measures
153 each gene's contribution to the covariance within two replicate screens and summarizes
154 the resulting values across all available screen pairs (replicate 1-2, 1-3, 2-3) (Methods,
155 **Table S1**). This analysis confirms that both the strongest positive and negative qGI scores
156 were highly reproducible across independent screens (**Figure S1g**). In particular, the most
157 reproducible negative GIs with *FASN* were interactions with *SLCO4A1*, *PGRMC2*, *LDLR*,
158 *RABL3* and *C12orf49* (**Figure S1g, Table S1**). We tested three of these top five strongest
159 negative GIs by independent validation assays and confirmed all three, examining WT
160 and *FASN*-KO HAP1 cells expressing gRNAs against *SLCO4A1*, *LDLR* and *C12orf49*
161 (**Figure 1e, S1h**).

162

163 To generate an aggregate set of *FASN* GIs, we mean-summarised qGI scores across the
164 three replicate screens (**Figure 1f, Table S2**). At a pathway level, significant negative GIs
165 ($qGI < -0.5$, $FDR < 0.5$) with *FASN* were strongly enriched for genes annotated with roles
166 in protein glycosylation, vesicle transport and cholesterol metabolism ($FDR < 0.05$) (**Figure**
167 **1g, Table S3**). In the global yeast genetic network negative GIs often connect functionally
168 related genes (Costanzo *et al*, 2010, 2016), and we observed a similar general trend for
169 the *FASN* negative GIs. For example, the *FASN* negative GIs included genes with
170 established roles in the uptake, transport, and breakdown of low density lipoprotein (LDL),

171 a major extracellular source of lipids, including the LDL receptor (*LDLR*) itself and its
172 coreceptor adaptor protein (*LDLRAP1*). We also observed negative GIs between *FASN*
173 and the transcription factor *SREBF2*, which controls expression of *LDLR*, as well as
174 *SCAP*, *MBTPS1* and *MBTPS2*, all of which are important for the activation and nuclear
175 translocation of *SREBF2* upon cholesterol depletion (**Figure 1h**). Moreover, we observed
176 negative GIs with additional lipid metabolic processes such as cholesterol biosynthesis
177 (*ACAT2*), genes functioning in long chain fatty acid activation and β -oxidation (*ACSL1*,
178 *ACSL3*), and vesicle trafficking genes (*RAB18/10/1A*, *RABGEF1*, *RAB3GAP2/1*) (**Figures**
179 **1h, S1i**), as well as a positive GI with the gene encoding stearoyl-CoA desaturase (*SCD*),
180 the product of which catalyses the rate-limiting step in the biosynthesis of
181 monounsaturated fatty acids.

182

183 The *FASN* screen also highlighted an enrichment for genes functioning in protein N-linked
184 glycosylation (e.g. *ALG3/8/9/12*, *MOGS*, *DOLPP1*, *PRKCSH*, *MGAT2*) (**Figures 1g-h,**
185 **S1i**). Interestingly, the hexosamine biosynthetic and N-linked glycosylation pathways have
186 been implicated in facilitating lipid accumulation from environmental sources through
187 direct modulation of N-glycan branching on fatty acid transporters, possibly explaining the
188 strong GIs we observe (Ryczko *et al*, 2016). N-linked glycosylation is also known to play
189 an important role in the activity of *LDLR* and activation of the *SREBP* transcriptional
190 programs, providing a potential explanation for the interaction between loss of *FASN* and
191 the glycosylation pathway (Cheng *et al*, 2015; Wang *et al*, 2018). Finally, we observed a
192 significant negative GI between *FASN* and *SLCO4A1* (**Figures 1f, S1g**). *SLCO4A1*
193 encodes a member of the organic anion-transporting polypeptides (OATPs), which can
194 transport a wide range of structurally unrelated compounds including hormones, bile acids
195 and lipid species (prostaglandins) (Obaidat *et al*, 2012). To summarize, these results
196 suggest that in the absence of cell autonomous *de novo* fatty acid synthesis, cells depend

197 on uptake and breakdown of lipids from the environment or the synthesis of sterols, with
198 our data illuminating the genetic determinants of how cells rewire to meet the demand for
199 lipids in proliferating cells.

200

201 **Expanding the genetic interaction landscape of *de novo* fatty acid synthesis**

202 To better understand the GI landscape of *de novo* fatty acid synthesis, we next performed
203 pooled genome-wide CRISPR screens using the TKOv3 library in five additional
204 coisogenic cell lines harbouring genetic KO of genes that exhibited significant negative
205 GIs with our *FASN*-KO query, including *LDLR*, *C12orf49* and *SREBF2* (**Table S2**), as well
206 as two genes that did not show a negative GI with *FASN*, including *SREBF1*, which
207 regulates the expression of *FASN* and other *de novo* fatty acid genes, and *ACACA*, which
208 functions in the same pathway and immediately upstream of *FASN* (**Figure 2a**) (Röhrig &
209 Schulze, 2016; Currie *et al*, 2013; Horton *et al*, 2008). Each of these five query gene
210 screens was performed in technical triplicate (i.e. parallel cultures from a common
211 infection). Since these additional GI screens were performed under the same conditions
212 as we used for the *FASN*-KO screens, we applied the same confidence threshold on the
213 derived qGI scores ($|qGI| > 0.5$, FDR < 0.5; Methods) (**Figures 2b-f, S2a-b, Table S2**). At
214 this confidence threshold, we estimated a per-screen false discovery rate of ~0.3 and a
215 false negative rate of ~0.6 (Methods; **Figure S1j**).

216

217 We next analyzed the functional enrichment across all GIs identified by our fatty acid
218 synthesis-related query screens. While the positive GIs were not functionally informative
219 in general, we observed a clear 5-fold enrichment of negative GIs for genes annotated to
220 functionally relevant pathways, which were defined by the metabolism-focused
221 HumanCyc standard (**Figure S2c**) (Romero *et al*, 2005). We further quantified enrichment
222 for pathways annotated at different levels of the HumanCyc database hierarchy, including

223 gene sets corresponding to general metabolic reaction categories, sub-categories, and
224 finally specific metabolic pathways (**Table S4**). At the most general level of the HumanCyc
225 pathway hierarchy, negative GIs from all six genome-wide screens were most enriched
226 for genes annotated to the biosynthesis and macromolecule modifications pathway
227 categories (**Figure 3a**). Further analysis of these terms at a more specific level of the
228 HumanCyc hierarchy (i.e. sub-category level), we found that genes exhibiting negative
229 GIs were associated with functions related to the roles of our six query genes, including
230 fatty acid, lipid and carbohydrate biosynthesis (**Figures 3b, S3a**). At a more refined level
231 of functional specificity within the fatty acid and lipid biosynthesis pathway, we found that
232 each query gene was associated with a significant enrichment for negative GIs with
233 functionally-related genes of distinct pathways. For example, the *LDLR* GI profile includes
234 negative GIs with genes in the cholesterol/epoxysqualene biosynthesis pathway (i.e.
235 *HMGCS1*, *MSMO1*, *HMGCR*, *FDFT1*, *NSDHL*, *HSD17B7*, *SQLE*, *HSD17B7*, *ACT2*,
236 *SQLE*, *LSS*) and the *ACACA*, *LDLR* and *SREBF2* GI profiles include negative GIs with
237 fatty acid elongation and biosynthesis pathway genes (*FASN*, *ACACA*, *OXSM*) (**Figures**
238 **3c-d**). Notably, the *FASN* GI profile, and to a lesser extent the *ACACA* and *LDLR* GI
239 profiles, revealed negative GIs with pathways and genes involved in N-glycosylation
240 initiation (*ALG6*, *ALG13*, *ALG11*, *ALG1*, *ALG2*, *ALG8*, *ALG5*, *ALG3*, *ALG12*, *ALG9*),
241 processing (*MOGS*, *PRKCSH*), dolichol monophosphate mannose synthase activity
242 (*DPM2*, *DPM3*, *DPM1*), and glycan transfer (*STT3A*, *STT3B*) (**Figures 3c,e, Table S4**).

243

244 Our survey of GIs related to perturbation of *de novo* fatty acid synthesis or exogenous
245 fatty acid uptake pathways provided unique insight into the genetic regulation of these
246 processes. Specifically, for the *SREBF2* screen, while we observed negative GIs with lipid
247 uptake genes such as *LDLR* and *LDLRAP1* (**Figure 3f, Table S2**), none were observed
248 with the cholesterol biosynthesis pathway (**Figures 3d, 2e**). This observation is consistent

249 with *SREBF2* being the predominant transcriptional regulator of cholesterol homeostasis
250 (Horton *et al*, 2008); its perturbation does not further reduce cellular fitness in cells
251 deficient for cholesterol biosynthesis. In addition, we also detected a strong positive GI
252 between *SREBF2* and *TFAP2C* (**Figure 2c**). Indeed, the *TFAP2* transcription factor family
253 has recently been proposed as a ‘master’ regulator of lipid droplet biogenesis (Scott *et al*,
254 2018), with our data suggesting that reduced sequestration of lipids into lipid droplets may
255 benefit *SREBF2*-KO cells to mitigate lipid starvation.

256

257 In contrast, *SREBF1* did not show enrichment for GIs for either the cholesterol or fatty acid
258 synthesis pathways (**Figure 3c, Table S2**). Instead, this query was found to show only a
259 strong reciprocal negative GI with its paralog *SREBF2*, highlighting the functional
260 redundancy between the paralog pair (**Figure 2e, Table S2**) and suggesting that *SREBF2*
261 may regulate some of the transcriptional targets of *SREBF1* as previously described
262 previously (Shimano & Sato, 2017; Horton *et al.*, 2008). Furthermore, the imbalanced
263 number of GIs between *SREBF1* and *SREBF2* may point towards asymmetric paralog
264 evolution, whereby duplicated genes gain or lose functional roles at different rates while
265 maintaining partially redundant functions, a process previously observed in yeast and
266 human cells (Zhou *et al*, 2014; VanderSluis *et al*, 2010; Ascencio *et al*, 2017).

267

268 **A novel role for *C12orf49* in lipid biosynthesis**

269 One of the strongest negative GIs identified in both the *FASN* and the *ACACA* profiles
270 involved the uncharacterized gene *C12orf49*, suggesting that this gene may have a role
271 in lipid metabolism (**Figures 1f, 2d, Table S2**). *C12orf49* is a 23.5 kDa protein that is part
272 of the UPF0454 family of uncharacterized proteins, contains an N-terminal
273 transmembrane sequence, single uncharacterized DUF2054 domain of approximately
274 200 amino acid residues, 14 conserved cysteines three of which are annotated to form

275 CC-dimers, and a predicted glycosylation site (The UniProt Consortium, 2019)(**Figure**
276 **S4a**). In some plant proteins, the uncharacterized UPF0454 is found situated next to a
277 glycosyltransferase domain and thus may be targeted into the lumen of the ER or Golgi
278 (Mitchell *et al*, 2019). By extension, the bulk of the C12orf49 protein may reside in the
279 lumen of the ER or Golgi. In addition, C12orf49 is ubiquitously expressed across tissues
280 and cell lines (<http://www.proteinatlas.org>) (Uhlen *et al*, 2015)). Notably, expression of
281 *C12orf49* is associated with differential prognoses on univariate analysis of TCGA data
282 across multiple tumor types, including kidney, breast, liver and sarcoma (**Figures S4b-e**;
283 $p < 0.05$) (Nagy *et al*, 2018), which further motivated us to study the functional role of this
284 previously uncharacterized gene.

285

286 Genetic interactions derived from a genome-wide screen using a *C12orf49*-KO query cell
287 line further supported a role for this gene in lipid biogenesis. Consistent with the results
288 described above, *C12orf49* showed a strong negative GI with both *FASN* and *ACACA*
289 (**Figure 2f**). *C12orf49* also showed negative GIs with *LDLR*, *ACSL1* (i.e. encoding acyl-
290 CoA synthase), *SLC25A1* (i.e. encoding mitochondrial citrate transporter), *SCD* and
291 *SREBF2* further supporting a role for this gene in fatty acid biosynthesis (**Figure 2f**).
292 Consistently, *C12orf49* negative GIs were enriched for genes involved in fatty acid
293 metabolism, cholesterol biosynthesis and additional metabolic pathways (FDR < 0.05)
294 (**Figure 4a, Table S3**). Moreover, as observed for the *FASN* GI profile, *C12orf49* negative
295 GIs involved genes functioning in vesicle-mediated trafficking and endocytosis, including
296 *RAB3GAP2*, *RABIF*, *RAB18*, *VPS18*, *VPS419* and *VPS39* (**Table S2**). Beyond vesicle
297 trafficking, many of the genes that showed a negative GI with *C12orf49* also displayed
298 negative GIs with other query genes in our lipid metabolism panel (e.g. *LDLR*, *ALG3*,
299 *ASCL1*, *MBTPS2*, *SLC25A1*, *PDHA1*), supporting the functional relatedness of these

300 genes (**Figures 4b-c, S4f-h**). Thus, our lipid metabolism GI map strongly implicates
301 *C12orf49* as playing a functional role in lipid metabolism.

302

303 To further confirm the predictions about *C12orf49*'s function based on our HAP1 GI data,
304 we also examined publicly available data from the 19Q2 DepMap release and observed
305 that *C12orf49* is essential for fitness in 120 out of 563 cell lines with highest dependencies
306 observed for lung, ovarian, pancreatic, colon and bile duct origins (Meyers *et al*, 2017;
307 Behan *et al*, 2019). Other genes that shared similar cell line essentiality profiles to
308 *C12orf49* included *SREBF1*, *SREBF2*, *MBTPS1*, *SCAP*, *SCD* and *ACSL3* (**Figures 4d**,
309 **S4i**). The association of *C12orf49* with lipid metabolism genes was corroborated by a
310 pathway enrichment analysis of the co-essentiality profiles, which revealed strong
311 enrichment for genes annotated to ultra-long-chain fatty acid biosynthesis (**Figures 4e**,
312 **S4j**). Interestingly, germline variants in *C12orf49* have also been reported to associate
313 with serum lipid abnormalities in high-density lipoprotein (HDL) in a multi-ethnic cohort of
314 the Million Veteran Program, further supporting a role for this gene in lipid metabolism
315 (Klarin *et al*, 2018). Overall, these observations support a novel function for *C12orf49* in
316 lipid metabolism that is conserved across diverse cell types.

317

318 ***C12orf49* is a novel regulator of lipid uptake**

319 We performed proximity-based labelling of proteins coupled to mass spectrometry (BioID-
320 MS) to reveal potential *C12orf49* protein interactions. Because the *C12orf49* single
321 predicted N-terminal transmembrane domain may direct the C-terminal DUF2054 domain
322 into the lumen of the secretory pathway, leaving the N-terminus facing the cytoplasm,
323 BioID-MS was performed separately with both N- and C-terminal BirA-tagged *C12orf49*
324 open reading frames (ORFs) expressed in HEK293 cells. Proximity-based labelling with
325 the N-terminal construct captured proteins localizing to various cellular compartments

326 including the ER, Golgi apparatus, plasma membrane and the cytosol, whereas the C-
327 terminal BirA construct revealed a strong enrichment of proteins localizing to the
328 endoplasmic reticulum (ER) lumen (**Figure 5a, Table S5**). Furthermore, the BirA ligase
329 fused to the N-terminal BirA ligase captured proximal interactions with proteins functioning
330 in vesicle and ER – Golgi transport, whereas C-terminus labelled proteins enriched for
331 functions related to protein folding and glycosylation (**Figure 5b, Table S6**). Together,
332 these results further support that C12orf49 localizes to the ER membrane or transport
333 vesicles that may traffic to or from the ER, whereby its N-terminus likely faces the
334 cytoplasm and, in this context, the C-terminus would face the ER lumen.

335

336 We performed immunofluorescence analysis to study the subcellular localization of
337 C12orf49 under normal and starved conditions. Under normal growth conditions (with
338 serum), C12orf49 containing a C-terminal V5 tag (i.e. C12orf49-V5) was localized
339 throughout the ER-Golgi network (**Figure 5c**), consistent with our BioID results. Strikingly,
340 C12orf49-V5 accumulated in the Golgi apparatus under serum starvation, as assessed by
341 co-staining with GOLGA2, a Golgi membrane marker protein (**Figure 5c**). These data thus
342 suggest that localization of C12orf49 is regulated in a growth condition-dependent
343 manner, involving the shuttling between the ER and the Golgi apparatus.

344

345 Together, genetic and proteomic interaction data indicate that C12orf49 may play a role
346 in lipid metabolism and vesicle-mediated transport. To explore this hypothesis, we
347 measured uptake of labelled LDL particles, which represent one of the major sources of
348 extracellular fatty acids, across several HAP1 KO lines. As expected, loss of *LDLR*
349 resulted in abolishment of LDL-staining, while *FASN*-KO cells displayed increased uptake
350 of exogenous lipid (**Figures 5d, S5a**). In contrast, loss of *C12orf49* caused a significant
351 reduction of LDL uptake, which was rescued by the exogenous expression of C12orf49

352 **(Figures 5d, S5a)**. Because since *C12orf49*-KO cells do not exhibit reduced uptake of
353 labelled transferrin **(Figure S5b)**, the reduction of LDL uptake is specific to lipid transport
354 and is not a consequence of a general defect in receptor-mediated endocytosis.,
355 Interestingly, a similar reduction in LDL uptake was also observed in *SREBF1*- and
356 *SREBF2*- deficient cells. Overall, these results indicate that *C12orf49* impacts LDL uptake
357 and support the GIs identified between *C12orf49* and genes functioning in fatty acid
358 biosynthesis and lipid homeostasis.

359

360 Sterol regulatory element-binding proteins (SREBPs) traffic to the Golgi where they are
361 cleaved such that the processed form enters the nucleus to activate transcription of
362 genes regulating lipid homeostasis (Brown & Goldstein, 1997; Horton *et al*, 2008). Thus,
363 *C12orf49* could somehow play a role in the activation of the SREBP transcription factors.
364 To explore this possibility, we performed RNA-sequencing experiments under normal and
365 serum-starved conditions across HAP1 WT, *C12orf49*-KO and *SREBF2*-KO cells **(Table**
366 **S7)**. As expected, serum-starvation resulted in induction of a cholesterol biosynthetic
367 transcriptomic signature in HAP1 WT cells but not in *SREBF2*-KO cells **(Figures 5e, S5c-**
368 **d)**. In *C12orf49*-KO cells, we observed a SREBP-mediated transcriptional response
369 similar to WT cells, suggesting that *C12orf49* is not absolutely required for the activation
370 of SREBP upon serum starvation **(Figure 5e, S5c-d)**. However, we did notice a trend for
371 lower expression of cholesterol biosynthesis and LDL uptake genes in *C12orf49*-KO cells,
372 which was confirmed by qRT-PCR **(Figure 5e, S5e)**. The absence of strong gene
373 expression changes suggests that *C12orf49* may also regulate LDL uptake on a post-
374 transcriptional level. We therefore measured LDLR protein levels on the cell surface by
375 flow cytometry but we did not observe any significant changes in LDLR localization or
376 abundance in *C12orf49*-KO compared to WT cells **(Figure S5f)**. Thus, *C12orf49* may

377 influence LDL uptake through the regulation of post-translational modifications of LDLR,
378 such as glycosylation, which takes place in the ER and Golgi apparatus (**Figure 5f**).

379

380 In summary, our unbiased GI screens and follow-up experiments have revealed that the
381 uncharacterized gene *C12orf49* plays a role in the regulation of lipid transport and our
382 data further indicate that its subcellular localization is dynamically regulated in a growth
383 condition-dependent manner throughout the ER-Golgi network. Our findings indicate that
384 *C12orf49* mainly regulates lipid uptake on a post-transcriptional level and we suggest that
385 *C12orf49* be named *LUR1* for its role in Lipid Uptake Biology. We speculate that the *LUR1*
386 product may be involved in some aspect of the glycosylation of LDLR, the recycling of
387 vesicles to the cell surface, or in regulating the transcriptional response mediated by
388 SREBPs (**Figure 5f**).

389 DISCUSSION

390 The systematic mapping of GIs in model organisms like yeast has provided a detailed
391 view into the functional organisation of eukaryotic cells (Costanzo *et al*, 2019). Recent
392 advances in CRISPR-based genome engineering technologies provide a path for similar
393 systematic GI studies in human cells (Horlbeck *et al*, 2018; Najm *et al*, 2018; Han *et al*,
394 2017; Norman *et al*, 2019; Shen *et al*, 2017). Here, we apply genome-wide CRISPR-based
395 fitness screens using query mutant HAP1 cell lines to systematically map GIs with a focus
396 on lipid metabolism. Our data revealed a strong interaction between *de novo* fatty acid
397 synthesis and lipid uptake processes, highlighting a system that balances synthesizing
398 lipids intracellularly with their uptake from the extracellular environment. More generally,
399 this analysis confirms that relatively strong negative GIs identify functionally related genes,
400 mapping a functional wiring diagram for a particular cellular process.

401

402 We screened a *FASN* mutant query cell line multiple times and identified highly confident
403 negative GIs, many of which were involved in lipid metabolism. Perturbation of *de novo*
404 fatty acid synthesis has been suggested as a prominent cancer therapeutic approach and
405 multiple compounds targeting *FASN* are currently being tested in clinical trials; for
406 example, TVB-2640 is a *FASN* inhibitor that is being tested in solid tumors in phase 2
407 trials, while both Fatostatin and Betulin are inhibitors of the SREBP-SCAP interaction in
408 pre-clinical development (Röhrig & Schulze, 2016; Brenner *et al*, 2017). Since single agent
409 therapies often lead to emergence of resistance and tumor relapse, it makes sense to
410 pursue therapeutic targets that are synergistic with *FASN* inhibition. Thus, the strong GIs
411 detected in our *FASN* screen may be informative towards future investigations of
412 combinatorial targets or biomarkers to treat diseases that would benefit from disruption of
413 *de novo* fatty acid biosynthesis.

414

415 Our focused GI landscape related to *de novo* fatty acid biosynthesis provides unique
416 insight into the genetic dependencies required for response to perturbation of lipid
417 metabolism. Several pathways emerge as being most commonly utilized to adapt to
418 perturbations, including those involved in alternate fatty acid and cholesterol biosynthesis
419 processes as well as lipid uptake. Interestingly, while our screens revealed strong negative
420 GIs between *de novo* fatty acid synthesis and uptake of LDL, we failed to detect
421 interactions with transporters of fatty acids. This may be a consequence of the genetic
422 redundancy inherent amongst the *SLC27A* (FATP) fatty acid transporter family (Gimeno,
423 2007). As previously shown in yeast (VanderSluis *et al*, 2010), functional redundancy
424 between paralogs can mask genetic interactions associated with perturbation of a single
425 gene of a duplicated pair and highlights an important need for multi-gene targeting
426 systems to survey complex genetic interactions involving more than two genes.
427 Nonetheless, our data suggest a strong functional relationship between *de novo* fatty acid
428 synthesis and glycosylation, and may involve a mechanism wherein cells modify the FATP
429 transporters through N-glycosylation, thereby enhancing lipid uptake as suggested by
430 Ryczko *et al* (Ryczko *et al*, 2016). As such, this pathway serves as an obvious focal point
431 not only for ongoing mechanistic investigation but also therapeutic development for anti-
432 cancer strategies targeting *de novo* fatty acid synthesis.

433

434 Genome-wide GI profiling also revealed an important role for *LUR1* (*C12orf49*) in lipid
435 uptake. Interestingly, analysis of the DepMap data revealed that *LUR1* is essential in the
436 same set of cancer cell lines that also depend on other lipid biosynthesis-related genes
437 for viability, including *SREBF1*, *MBTPBS1*, *SCAP* and *SCD*. Similarly, two recent studies
438 identifying co-functional gene clusters, support a functional role of *LUR1* in lipid
439 metabolism across diverse genetic backgrounds (Boyle *et al*, 2018; Kim *et al*, 2019).
440 Furthermore, genome-wide association studies with large patient cohorts have found

441 *LUR1* variants linked to abnormal HDL profiles (Klarin *et al*, 2018), neuroticism (Luciano
442 *et al*, 2018; Kichaev *et al*, 2019; Nagel *et al*, 2018), body height (Kichaev *et al*, 2019), and
443 neuroticism (Nagel *et al*, 2018), all phenotypes that could have root causes in lipid
444 metabolism defects.

445

446 In summary, we provide an unbiased and genome-wide approach for uncovering genetic
447 vulnerabilities related to lipid metabolism in human cells, which led us to identify a function
448 for *LUR1*. Our GI profiles for *de novo* fatty acid synthesis and related lipid uptake genes
449 provide a resource for studying metabolic rewiring and disease phenotypes linked to lipid
450 metabolism. We also demonstrate the power of systematic GI profiling using query
451 mutants in a coisogenic cell line, an approach that can be applied to other bioprocesses
452 and expanded to begin generating more comprehensive GI maps for human genes.

453

454 **ACKNOWLEDGMENTS**

455 We thank members of the Moffat lab for helpful discussions. Queenie Huang and Shaan
456 Sidhu are gratefully acknowledged for assistance with molecular biology experiments.
457 M.A. was supported by a Swiss National Science Foundation Postdoctoral Fellowship;
458 K.A.L. was supported by a Vanier Canada Graduate Scholarship and Studentship award
459 from the Kidney Cancer Research Network of Canada. M.B. was supported by a DFG
460 Fellowship (Bi 2086/1-1). This research was funded by grants from the Canadian Institutes
461 for Health Research (J.M., C.B and B.A), Ontario Research Fund (B.A., C.B. and J.M) and
462 Canada Research Chairs Program (J.M. and C.B.). C.L.M., M.B., and M.R. are partially
463 supported by grants from the National Science Foundation (MCB 1818293) and the
464 National Institutes of Health (R01HG005084, R01HG005853).

465

466 **AUTHOR CONTRIBUTIONS**

467 Conceptualization and design of the study: M.A., K.A.L., and J.M.; Experimental
468 investigation: M.A., K.A.L., A.H.Y.T., K.C., L.N., O.S., A.H., J.P., Z.L., H.A. and A.W. Data
469 analysis: M.A., K.L., M.B., M.C., M.R., K.R.B., C.R., M.U., P.M., J.W.D, A.C.G, J.L.M and
470 J.M.; Writing & Editing: M.A., K.A.L., M.B., M.C., B.J.A., C.B., C.L.M. and J.M. with the
471 input from other authors; Supervision: J.W.D., A.C.G., C.L.M., B.J.A., C.B., and J.M.;
472 Funding Acquisition: C.L.M., B.J.A., C.B. and J.M..

473

474 **COMPETING INTERESTS STATEMENT**

475 J.M., B.A. and C.B are shareholders in Northern Biologics. J.M. is a sharehold in Pionyr
476 Immunotherapeutics, is acting CSO and shareholder in Empirica Therapeutics, and is an
477 SAB member and shareholder of Aelian Biotechnology. C.B. is an SAB member of of
478 Yumanity Therapeutics. The authors declare no competing interest.

479

480

481 **REFERENCES**

- 482 Aregger M, Chandrashekar M, Tong AHY, Chan K & Moffat J (2019) Pooled Lentiviral
483 CRISPR-Cas9 Screens for Functional Genomics in Mammalian Cells. *Methods Mol.*
484 *Biol.* **1869**: 169–188
- 485 Ascencio D, Ochoa S, Delaye L & DeLuna A (2017) Increased rates of protein evolution
486 and asymmetric deceleration after the whole-genome duplication in yeasts. *BMC*
487 *Evol. Biol.* **17**: 40
- 488 Ashburner M, Ball CA, Blake JA, Botstein D, Butler H, Cherry JM, Davis AP, Dolinski K,
489 Dwight SS, Eppig JT, Harris MA, Hill DP, Issel-Tarver L, Kasarskis A, Lewis S,
490 Matese JC, Richardson JE, Ringwald M, Rubin GM & Sherlock G (2000) Gene
491 Ontology: tool for the unification of biology. *Nat. Genet.* **25**: 25–29
- 492 Behan FM, Iorio F, Picco G, Gonçalves E, Beaver CM, Migliardi G, Santos R, Rao Y, Sassi
493 F, Pinnelli M, Ansari R, Harper S, Jackson DA, McRae R, Pooley R, Wilkinson P, van
494 der Meer D, Dow D, Buser-Doepner C, Bertotti A, et al (2019) Prioritization of cancer
495 therapeutic targets using CRISPR–Cas9 screens. *Nature* **568**: 511–516
- 496 Benjamin DI, Li DS, Lowe W, Heuer T, Kemble G & Nomura DK (2015) Diacylglycerol
497 Metabolism and Signaling Is a Driving Force Underlying FASN Inhibitor Sensitivity in
498 Cancer Cells. *ACS Chem. Biol.* **10**: 1616–1623
- 499 Billmann M, Chaudhary V, ElMaghraby MF, Fischer B & Boutros M (2018) Widespread
500 Rewiring of Genetic Networks upon Cancer Signaling Pathway Activation. *Cell Syst.*
501 **6**: 52-64.e4
- 502 Birsoy K, Possemato R, Lorbeer FK, Bayraktar EC, Thiru P, Yucel B, Wang T, Chen WW,
503 Clish CB & Sabatini DM (2014) Metabolic determinants of cancer cell sensitivity to
504 glucose limitation and biguanides. *Nature* **508**: 108–12
- 505 Birsoy K, Wang T, Chen WW, Freinkman E, Abu-Remaileh M & Sabatini DM (2015) An
506 Essential Role of the Mitochondrial Electron Transport Chain in Cell Proliferation Is
507 to Enable Aspartate Synthesis. *Cell* **162**: 540–551
- 508 Boyle EA, Pritchard JK & Greenleaf WJ (2018) High-resolution mapping of cancer cell
509 networks using co-functional interactions. *Mol. Syst. Biol.* **14**: e8594
- 510 Brenner A, Falchook G, Patel M, Infante J, Arkenau H-T, Dean E, Borazanci E, Lopez J,
511 Moore K, Schmid P, Frankel A, Jones S, McCulloch W, Kemble G, Grimmer K &
512 Burris H (2017) Abstract P6-11-09: Heavily pre-treated breast cancer patients show
513 promising responses in the first in human study of the first-in-class fatty acid synthase
514 (FASN) inhibitor, TVB-2640 in combination with paclitaxel. In *Cancer Research* pp

515 P6-11-09-P6-11-09. American Association for Cancer Research
516 Brown MS & Goldstein JL (1997) The SREBP pathway: Regulation of cholesterol
517 metabolism by proteolysis of a membrane-bound transcription factor. *Cell* **89**: 331–
518 340
519 Carette JE, Raaben M, Wong AC, Herbert AS, Obernosterer G, Mulherkar N, Kuehne AI,
520 Kranzusch PJ, Griffin AM, Ruthel G, Dal Cin P, Dye JM, Whelan SP, Chandran K &
521 Brummelkamp TR (2011) Ebola virus entry requires the cholesterol transporter
522 Niemann-Pick C1. *Nature* **477**: 340–3
523 Chen M & Huang J (2019) The expanded role of fatty acid metabolism in cancer: new
524 aspects and targets. *Precis. Clin. Med.* **2**: 183–191
525 Chen RR, Yung MMH, Xuan Y, Zhan S, Leung LL, Liang RR, Leung THY, Yang H, Xu D,
526 Sharma R, Chan KKL, Ngu S-F, Ngan HYS & Chan DW (2019) Targeting of lipid
527 metabolism with a metabolic inhibitor cocktail eradicates peritoneal metastases in
528 ovarian cancer cells. *Commun. Biol.* **2**: 281
529 Cheng C, Ru P, Geng F, Liu J, Yoo JY, Wu X, Cheng X, Euthine V, Hu P, Guo JY, Lefai
530 E, Kaur B, Nohturfft A, Ma J, Chakravarti A & Guo D (2015) Glucose-Mediated N-
531 glycosylation of SCAP Is Essential for SREBP-1 Activation and Tumor Growth.
532 *Cancer Cell* **28**: 569–581
533 Costanzo M, Baryshnikova A, Bellay J, Kim Y, Spear ED, Sevier CS, Ding H, Koh JLY,
534 Toufighi K, Mostafavi S, Prinz J, St Onge RP, VanderSluis B, Makhnevych T,
535 Vizeacoumar FJ, Alizadeh S, Bahr S, Brost RL, Chen Y, Cokol M, et al (2010) The
536 genetic landscape of a cell. *Science* **327**: 425–31
537 Costanzo M, Kuzmin E, van Leeuwen J, Mair B, Moffat J, Boone C & Andrews B (2019)
538 Global Genetic Networks and the Genotype-to-Phenotype Relationship. *Cell* **177**:
539 85–100
540 Costanzo M, VanderSluis B, Koch EN, Baryshnikova A, Pons C, Tan G, Wang W, Usaj M,
541 Hanchard J, Lee SD, Pelechano V, Styles EB, Billmann M, Van Leeuwen J, Van Dyk
542 N, Lin ZY, Kuzmin E, Nelson J, Piotrowski JS, Srikumar T, et al (2016) A global
543 genetic interaction network maps a wiring diagram of cellular function. *Science* **353**:
544 aaf1420–aaf1420
545 Currie E, Schulze A, Zechner R, Walther TC & Farese RV (2013) Cellular Fatty Acid
546 Metabolism and Cancer. *Cell Metab.* **18**: 153–161
547 Doench JG (2018) Am i ready for CRISPR? A user's guide to genetic screens. *Nat. Rev.*
548 *Genet.* **19**: 67–80

- 549 Fischer B, Sandmann T, Horn T, Billmann M, Chaudhary V, Huber W & Boutros M (2015)
550 A map of directional genetic interactions in a metazoan cell. *Elife* **4**:
551 Garber K (2016) Cancer anabolic metabolism inhibitors move into clinic. *Nat. Biotechnol.*
552 **34**: 794–795
553 Gimeno RE (2007) Fatty acid transport proteins. *Curr. Opin. Lipidol.* **18**: 271–6
554 Greene CS, Krishnan A, Wong AK, Ricciotti E, Zelaya RA, Himmelstein DS, Zhang R,
555 Hartmann BM, Zaslavsky E, Sealfon SC, Chasman DI, FitzGerald GA, Dolinski K,
556 Grosser T & Troyanskaya OG (2015) Understanding multicellular function and
557 disease with human tissue-specific networks. *Nat. Genet.* **47**: 569–576
558 Han K, Jeng EE, Hess GT, Morgens DW, Li A & Bassik MC (2017) Synergistic drug
559 combinations for cancer identified in a CRISPR screen for pairwise genetic
560 interactions. *Nat. Biotechnol.* **35**: 463–474
561 Harrison R, Papp B, Pál C, Oliver SG & Delneri D (2007) Plasticity of genetic interactions
562 in metabolic networks of yeast. *Proc. Natl. Acad. Sci. U. S. A.* **104**: 2307–12
563 Hart T, Chandrashekhar M, Aregger M, Steinhart Z, Brown KR, MacLeod G, Mis M,
564 Zimmermann M, Fradet-Turcotte A, Sun S, Mero P, Dirks P, Sidhu S, Roth FP,
565 Rissland OS, Durocher D, Angers S & Moffat J (2015) High-Resolution CRISPR
566 Screens Reveal Fitness Genes and Genotype-Specific Cancer Liabilities. *Cell* **163**:
567 1515–26
568 Hart T, Tong AHY, Chan K, Van Leeuwen J, Seetharaman A, Aregger M, Chandrashekhar
569 M, Hustedt N, Seth S, Noonan A, Habsid A, Sizova O, Nedyalkova LL, Climie R,
570 Tworzyanski L, Lawson K, Sartori MA, Alibeh S, Tieu D, Masud S, et al (2017)
571 Evaluation and Design of Genome-Wide CRISPR/SpCas9 Knockout Screens. *G3*
572 *Genes, Genomes, Genet.* **7**: g3.117.041277
573 Hesketh GG, Youn JY, Samavarchi-Tehrani P, Raught B & Gingras AC (2017) Parallel
574 exploration of interaction space by BioID and affinity purification coupled to mass
575 spectrometry. In *Methods in Molecular Biology* pp 115–136. Humana Press, New
576 York, NY
577 Horlbeck MA, Xu A, Wang M, Bennett NK, Park CY, Bogdanoff D, Adamson B, Chow ED,
578 Kampmann M, Peterson TR, Nakamura K, Fischbach MA, Weissman JS & Gilbert
579 LA (2018) Mapping the Genetic Landscape of Human Cells. *Cell* **174**: 953-967.e22
580 Horton JD, Goldstein JL & Brown MS (2008) SREBPs: activators of the complete program
581 of cholesterol and fatty acid synthesis in the liver. *J. Clin. Invest.* **109**: 1125–1131
582 Imoto M (2018) Chemistry and biology for the small molecules targeting characteristics of

583 cancer cells. *Biosci. Biotechnol. Biochem.* **83**: 1–10

584 Jones SF & Infante JR (2015) Molecular Pathways: Fatty Acid Synthase. *Clin. Cancer*
585 *Res.* **21**: 5434–5438

586 Kichaev G, Bhatia G, Loh P-R, Gazal S, Burch K, Freund MK, Schoech A, Pasaniuc B &
587 Price AL (2019) Leveraging Polygenic Functional Enrichment to Improve GWAS
588 Power. *Am. J. Hum. Genet.* **104**: 65–75

589 Kim E, Dede M, Lenoir WF, Wang G, Srinivasan S, Colic M & Hart T (2019) A network of
590 human functional gene interactions from knockout fitness screens in cancer cells.
591 *Life Sci. alliance* **2**: e201800278

592 Klarin D, Damrauer SM, Cho K, Sun Y V., Teslovich TM, Honerlaw J, Gagnon DR, DuVall
593 SL, Li J, Peloso GM, Chaffin M, Small AM, Huang J, Tang H, Lynch JA, Ho Y-L, Liu
594 DJ, Emdin CA, Li AH, Huffman JE, et al (2018) Genetics of blood lipids among
595 ~300,000 multi-ethnic participants of the Million Veteran Program. *Nat. Genet.* **50**:
596 1514–1523

597 Liberzon A, Subramanian A, Pinchback R, Thorvaldsdottir H, Tamayo P & Mesirov JP
598 (2011) Molecular signatures database (MSigDB) 3.0. *Bioinformatics* **27**: 1739–1740

599 Liu G, Knight JDR, Zhang JP, Tsou C-C, Wang J, Lambert J-P, Larsen B, Tyers M, Raught
600 B, Bandeira N, Nesvizhskii AI, Choi H & Gingras A-C (2016) Data Independent
601 Acquisition analysis in ProHits 4.0. *J. Proteomics* **149**: 64–68

602 Luciano M, Hagenaars SP, Davies G, Hill WD, Clarke T-K, Shirali M, Harris SE, Marioni
603 RE, Liewald DC, Fawns-Ritchie C, Adams MJ, Howard DM, Lewis CM, Gale CR,
604 McIntosh AM & Deary IJ (2018) Association analysis in over 329,000 individuals
605 identifies 116 independent variants influencing neuroticism. *Nat. Genet.* **50**: 6–11

606 Menendez JA & Lupu R (2017) Fatty acid synthase (FASN) as a therapeutic target in
607 breast cancer. *Expert Opin. Ther. Targets* **21**: 1001–1016

608 Meyers RM, Bryan JG, McFarland JM, Weir BA, Sizemore AE, Xu H, Dharia N V,
609 Montgomery PG, Cowley GS, Pantel S, Goodale A, Lee Y, Ali LD, Jiang G, Lubonja
610 R, Harrington WF, Strickland M, Wu T, Hawes DC, Zhivich VA, et al (2017)
611 Computational correction of copy number effect improves specificity of CRISPR-
612 Cas9 essentiality screens in cancer cells. *Nat. Genet.* **49**: 1779–1784

613 Mitchell AL, Attwood TK, Babbitt PC, Blum M, Bork P, Bridge A, Brown SD, Chang H-Y,
614 El-Gebali S, Fraser MI, Gough J, Haft DR, Huang H, Letunic I, Lopez R, Luciani A,
615 Madeira F, Marchler-Bauer A, Mi H, Natale DA, et al (2019) InterPro in 2019:
616 improving coverage, classification and access to protein sequence annotations.

- 617 *Nucleic Acids Res.* **47**: D351–D360
- 618 Nagel M, Watanabe K, Stringer S, Posthuma D & van der Sluis S (2018) Item-level
619 analyses reveal genetic heterogeneity in neuroticism. *Nat. Commun.* **9**: 905
- 620 Nagy Á, Lániczky A, Menyhárt O & Györfy B (2018) Validation of miRNA prognostic power
621 in hepatocellular carcinoma using expression data of independent datasets. *Sci. Rep.*
622 **8**: 9227
- 623 Najm FJ, Strand C, Donovan KF, Hegde M, Sanson KR, Vaimberg EW, Sullender ME,
624 Hartenian E, Kalani Z, Fusi N, Listgarten J, Younger ST, Bernstein BE, Root DE &
625 Doench JG (2018) Orthologous CRISPR-Cas9 enzymes for combinatorial genetic
626 screens. *Nat. Biotechnol.* **36**: 179–189
- 627 Norman TM, Horlbeck MA, Replogle JM, Ge AY, Xu A, Jost M, Gilbert LA & Weissman JS
628 (2019) Exploring genetic interaction manifolds constructed from rich single-cell
629 phenotypes. *Science* **365**: 786–793
- 630 Obaidat A, Roth M & Hagenbuch B (2012) The Expression and Function of Organic Anion
631 Transporting Polypeptides in Normal Tissues and in Cancer. *Annu. Rev. Pharmacol.*
632 *Toxicol.* **52**: 135–151
- 633 Röhrig F & Schulze A (2016) The multifaceted roles of fatty acid synthesis in cancer. *Nat.*
634 *Rev. Cancer* **16**: 732–749
- 635 Romero P, Wagg J, Green ML, Kaiser D, Krummenacker M & Karp PD (2005)
636 Computational prediction of human metabolic pathways from the complete human
637 genome. *Genome Biol.* **6**: R2
- 638 Ryczko MC, Pawling J, Chen R, Abdel Rahman AM, Yau K, Copeland JK, Zhang C,
639 Surendra A, Guttman DS, Figeys D & Dennis JW (2016) Metabolic Reprogramming
640 by Hexosamine Biosynthetic and Golgi N-Glycan Branching Pathways. *Sci. Rep.* **6**:
641 23043
- 642 Scott CC, Vossio S, Rougemont J & Gruenberg J (2018) TFAP2 transcription factors are
643 regulators of lipid droplet biogenesis. *Elife* **7**:
- 644 Shen JP, Zhao D, Sasik R, Luebeck J, Birmingham A, Bojorquez-Gomez A, Licon K,
645 Klepper K, Pekin D, Beckett AN, Sanchez KS, Thomas A, Kuo C-C, Du D, Roguev
646 A, Lewis NE, Chang AN, Kreisberg JF, Krogan N, Qi L, et al (2017) Combinatorial
647 CRISPR–Cas9 screens for de novo mapping of genetic interactions. *Nat. Methods*
648 **14**: 573–576
- 649 Szappanos B, Kovács K, Szamecz B, Honti F, Costanzo M, Baryshnikova A, Gelius-
650 Dietrich G, Lercher MJ, Jelasity M, Myers CL, Andrews BJ, Boone C, Oliver SG, Pál

- 651 C & Papp B (2011) An integrated approach to characterize genetic interaction
652 networks in yeast metabolism. *Nat. Genet.* **43**: 656–62
- 653 The UniProt Consortium (2019) UniProt: a worldwide hub of protein knowledge. *Nucleic*
654 *Acids Res.* **47**: D506–D515
- 655 Uhlen M, Fagerberg L, Hallstrom BM, Lindskog C, Oksvold P, Mardinoglu A, Sivertsson
656 A, Kampf C, Sjostedt E, Asplund A, Olsson I, Edlund K, Lundberg E, Navani S,
657 Szgyarto CA-K, Odeberg J, Djureinovic D, Takanen JO, Hober S, Alm T, et al (2015)
658 Tissue-based map of the human proteome. *Science* **347**: 1260419–1260419
- 659 VanderSluis B, Bellay J, Musso G, Costanzo M, Papp B, Vizeacoumar FJ, Baryshnikova
660 A, Andrews B, Boone C & Myers CL (2010) Genetic interactions reveal the
661 evolutionary trajectories of duplicate genes. *Mol. Syst. Biol.* **6**: 429
- 662 Wang S, Mao Y, Narimatsu Y, Ye Z, Tian W, Goth CK, Lira-Navarrete E, Pedersen NB,
663 Benito-Vicente A, Martin C, Uribe KB, Hurtado-Guerrero R, Christoffersen C, Seidah
664 NG, Nielsen R, Christensen EI, Hansen L, Bennett EP, Vakhrushev SY, Schjoldager
665 KT, et al (2018) Site-specific O-glycosylation of members of the low-density
666 lipoprotein receptor superfamily enhances ligand interactions. *J. Biol. Chem.* **293**:
667 7408–7422
- 668 Wright A V., Nuñez JK & Doudna JA (2016) Biology and Applications of CRISPR Systems:
669 Harnessing Nature’s Toolbox for Genome Engineering. *Cell* **164**: 29–44
- 670 Zhou Z, Zhou J, Su Z & Gu X (2014) Asymmetric Evolution of Human Transcription Factor
671 Regulatory Networks. *Mol. Biol. Evol.* **31**: 2149–2155
- 672

673 **METHODS**

674 **Cell culture**

675 Human HAP1 wild type cells were obtained from Horizon Genomics (clone C631, sex:
676 male with lost Y chromosome, RRID: CVCL_Y019). The following HAP1 gene knockout
677 cell lines were obtained from Horizon: *FASN* (HZGHC003700c006), *ACACA*
678 (HZGHC004903c002), *LDLR* (HZGHC003978c007), *SREBF1* (HZGHC001361c012),
679 *SREBF2* (HZGHC000683c004). All gene knockout cell lines were confirmed to carry the
680 expected out-of-frame insertions or deletions by Sanger Sequencing of PCR products.
681 HAP1 cells were maintained in low glucose (10 mM), low glutamine (1 mM) DMEM
682 (Wisent, 319-162-CL) supplemented with 10% FBS (Life Technologies) and 1%
683 Penicillin/Streptomycin (Life Technologies). This culture medium is referred to as “minimal
684 medium”. Cells were dissociated using Trypsin (Life Technologies) and all cells were
685 maintained at 37°C and 5% CO₂. Cells were regularly monitored for mycoplasma infection.
686

687 **HAP1 KO cell line generation**

688 The HAP1 *C12orf49* gene knockout cell line was constructed by first cloning a gRNA
689 targeting *C12orf49* (Table S8) into the pX459v2 backbone (Addgene #62988), which was
690 modified to carry the same restriction overhangs as the pLCKO vector (Addgene #73311).
691 350k HAP1 WT cells were seeded into a 6-well plate and 24 hours later cells were
692 transfected with a mix of 2 µg pX459 plasmid (Addgene #62988) carrying a gRNA, 6 µl X-
693 treme Gene transfection reagent (Roche), and 100 µl Opti-MEM media (Life
694 Technologies). Twenty-four hours after transfection, cells were selected in medium
695 containing 1 µg/ml puromycin for three days and single cells were sorted onto 96-well
696 plates by manual seeding of a single cell suspension at 0.6 cells/well. Following
697 amplification of cells from individual wells, genomic DNA was extracted with Extracta DNA
698 Prep (Quanta Bio), Sanger sequencing was performed across the gRNA target sites

699 following PCR amplification, and successful gene knockouts were identified following
700 sequence analysis.

701

702 **Library virus production and MOI determination**

703 For CRISPR library virus production, 8 million HEK293T cells were seeded per 15 cm
704 plate in DMEM medium containing high glucose, pyruvate and 10% FBS. Twenty-four
705 hours after seeding, the cells were transfected with a mix of 8 µg lentiviral lentiCRISPRv2
706 vector containing the TKOv3 gRNA library (Addgene #90294) (Hart *et al*, 2017), 4.8 µg
707 packaging vector psPAX2, 3.2 µg envelope vector pMD2.G, 48 µl X-treme Gene
708 transfection reagent (Roche) and 1.4 ml Opti-MEM media (Life Technologies). Twenty-
709 four hours after transfection, the media was replaced with serum-free, high-BSA growth
710 media (DMEM, 1.1g/100ml BSA, 1% Penicillin/Streptomycin). Virus-containing media was
711 harvested 48 hours after transfection, centrifuged at 1,500 rpm for 5 minutes, aliquoted
712 and frozen at -80°C.

713

714 For determination of viral titers, 3 million HAP1 cells seeded in 15 cm plates were
715 transduced with different dilutions of the TKOv3 lentiviral gRNA library along with
716 polybrene (8 µg/ml), in a total of 20 ml medium. After 24 hours, the virus-containing media
717 was replaced with 25 ml of fresh media containing puromycin (1 µg/ml), and cells were
718 incubated for an additional 48 hours. Multiplicity of infection (MOI) of the titrated virus was
719 determined 72 hours post-infection by comparing percent survival of puromycin-selected
720 cells to cells that were infected but not selected with puromycin (i.e. puro minus controls).

721

722 **Pooled CRISPR dropout screens**

723 For pooled CRISPR dropout screens, 3 million HAP1 cells were seeded in 15 cm plates
724 in 20 ml of specified media. A total of 90 million cells were transduced with the lentiviral
725 TKOv3 library at a MOI~0.3, such that each gRNA is represented in about 200-300 cells.
726 Twenty-four hours after infection, transduced cells were selected with 25 ml medium
727 containing 1 µg/ml puromycin for 48 hours. Cells were then harvested and pooled, and 30
728 million cells were collected for subsequent gDNA extraction and determination of the
729 library representation at day 0 (i.e. T0 reference). The pooled cells were then seeded into
730 three replicate plates, each containing 18 million cells (>200-fold library coverage), which
731 were passaged every three days and maintained at >200-fold library coverage until T18.
732 Genomic DNA pellets from each replicate were collected at each day of cell passage.

733

734 **Preparation of sequencing libraries and Illumina sequencing**

735 Genomic DNA was extracted using the Wizard Genomic DNA Purification Kit (Promega).
736 The gDNA pellets were resuspended in TE buffer, and the concentration was estimated
737 by Qubit using dsDNA Broad Range Assay reagents (Invitrogen). Sequencing libraries
738 were prepared from 50 µg of the extracted gDNA in two PCR steps, the first to enrich
739 guide-RNA regions from the genome, and the second to amplify guide-RNA and attach
740 Illumina TruSeq adapters with i5 and i7 indices as described previously using staggered
741 primers aligning in both orientations to the guide-RNA region (Table S8) (Aregger *et al*,
742 2019). Barcoded libraries were gel purified and final concentrations were estimated by
743 quantitative RT-PCR. Sequencing libraries were sequenced on an Illumina HiSeq2500
744 using single read sequencing and completed with standard primers for dual indexing with
745 HiSeq SBS Kit v4 reagents. The first 21 cycles of sequencing were dark cycles, or base
746 additions without imaging. The actual 36-bases read begins after the dark cycles and
747 contains two index reads, reading the i7 first, followed by i5 sequences. The T0 and T18
748 time point samples were sequenced at 400- and 200-fold library coverage, respectively.

749

750 **Construction of color-coded lentiCRISPRv2 vectors for co-culture assay**

751 The color-coded lentiCRISPRv2 vectors were derived from the lentiCRISPRv2 vector
752 (Addgene #52961) by inserting mCherry (Addgene #36084) or mClover3 (Addgene
753 #74236) open reading frames between the Cas9 and PuroR expression cassette. To this
754 end, the lentiCRISPRv2 vector was digested with BamHI, PCR products coding for the
755 respective fluorescent protein flanked by T2A and P2A self-cleaving peptides were ligated
756 into the vector using Gibson assembly. The two forward primers (Table S8) were used at
757 a 1:0.1:1 (P233:P234:P235) ratio in the same PCR reaction with the reverse primer
758 (primers bind to both fluorescent proteins mCherry and mClover3).

759

760 **Validation of genetic interactions using co-culture assays**

761 For validation of genetic interactions, HAP1 parental and gene knockout clones were
762 transduced with color-coded lentiCRISPRv2 vectors targeting either an intergenic site in
763 the AAVS1 locus (i.e. negative control), or a specific target gene hit (e.g. *LDLR*). Each
764 gene was targeted with three independent and unique gRNAs. Twenty-four hours after
765 transduction, cells were selected with 1 µg/ml puromycin for 48 hours and seeded for co-
766 culture proliferation assays as follow: 50k of green (e.g. lentiCRISPRv2-mClover3 *AAVS1*
767 gRNA) and red (e.g. lentiCRISPRv2-mCherry hit gene gRNA) cells were mixed (total
768 100k) in a 6-well plate in both color orientations for both parental and gene knockout cells,
769 respectively. Cells were passaged every 4 days until day 12 (T12). Cells were trypsinized,
770 washed and stained for dead cells using Zombie NIR (BioLegend). The relative proportion
771 of red and green cells in the co-culture were assessed using an LSR Fortessa flow
772 cytometer (BD Bioscience). The relative ratio of Hit:AAVS1 was calculated and averaged
773 for the three gene-targeting guides and two color orientations.

774

775 **Low-density lipoprotein and transferrin uptake assay**

776 For uptake experiments with labelled probes 150k HAP1 cells were seeded in a 12-well
777 plate. After 48 hours cells were serum-starved overnight in minimal medium (described
778 above) complemented with 0.3% BSA (BioShop) instead of FBS. After 16 hours cells were
779 labelled with Dil-LDL (Invitrogen L3482), pHrodo Red LDL (Invitrogen L34356) or pHrodo
780 Red Transferin (P35376) at 2 µg/ml (1:500) in minimal medium plus 0.3% BSA for 15
781 minutes at 37°C. Cells were washed in PBS, trypsinized and stained with 7-AAD
782 (BioLegend 420404) or Zombie NIR (BioLegend 423105) cell viability solution at 25 ng/ml
783 (1:2,000) for 5 minutes at room temperature. Staining was measured using an LSR
784 Fortessa flow cytometer (BD Bioscience).

785

786 **Proximity-based labelling of proteins capture to mass spectrometry (BioID-MS)**

787 BioID-MS analysis was performed essentially as described previously (Hesketh *et al*,
788 2017), with minor modifications. In brief, HEK293 Flp-In T-REx lines expressing inducible
789 N- or C-terminal BirA*-FLAG-tagged C12ORF49 open reading frames were generated.
790 Cells were treated with 1 µg/ml tetracycline to induce expression of baits and 50 µM biotin
791 for labelling of proximal proteins. After 24 hours cell pellets were collected and lysed in
792 RIPA lysis buffer (50mM Tris-HCl pH 7.5, 150mM NaCl, 0.1% (w/v) SDS, 1% NP-40, 1mM
793 EDTA, 1mM MgCl₂; 0.5% Deoxycholate and Sigma protease inhibitors were added right
794 before cell lysis.) at an 1:10 (g:ml) ratio, sonicated three times for 5 seconds with 2
795 seconds breaks. 1ul/sample TurboNuclease (BioVision) and 1ul/sample RNase (Sigma)
796 was added and samples were incubated at 4°C for 30 minutes. 20% SDS was added to
797 bring the sample's final SDS concentration to 0.25%, samples were mixed well and
798 centrifuged at 14,000 rpm (Microfuge) for 20 mins in 4°C. The supernatant was added to
799 Streptavidin resin (pre washed with lysis buffer) using 30µl bed volume and rotated at 4°C
800 for 3 hours. Beads were washed after binding as following: a) 1x1ml of 2% SDS buffer

801 (2% SDS, 50mM Tris-Hcl pH7.5), b) 1x1ml of lysis buffer, c) 1x1ml of HEK293 lysis buffer
802 (with 0.1% NP-40), d) 3x1ml of 50mM ammonium bicarbonate (made fresh). After
803 purification of biotinylated preys using streptavidin sepharose, samples were digested on
804 beads using trypsin. Samples were separated by liquid chromatography and analysed by
805 tandem mass spectrometry on a Thermo Orbitrap Elite mass spectrometer. Data
806 processing and analysis was performed within the ProHits LIMS (Liu *et al*, 2016) searched
807 against the RefSeq human and adenovirus data base, version 57; forward and reverse.
808 Mascot and Comet search results were jointly analysed using the iProphet component of
809 the Trans Proteomic Pipeline. High confidence interactions were determined by scoring
810 bait samples against negative control samples (8 negative controls consisting of either
811 BirA*-FLAG alone, BirA*-FLAG-EGFP, empty vector backbone or EGFP alone were
812 analysed; twelve samples for different baits, SLCO4A1, SLC35A1, UAP1L1 and C1orf115,
813 were also included in this analysis) using the statistical tool SAINTexpress v3.6.1 with two-
814 fold compression of the negative controls and default parameters). Preys with a SAINT
815 score (FDR) of less than 1% were considered as high confidence hits. All mass
816 spectrometry data will be deposited to ProteomeXchange through partner MassIVE
817 (massive.ucsd.edu) upon publication of manuscript.

818

819 **Western Blotting**

820 HAP1 WT and *FASN* KO cells were lysed in buffer F (10 mM Tris pH 7.05, 50 mM NaCl,
821 30 mM Na pyrophosphate, 50 mM NaF, 10% Glycerol, 0.5% Triton X-100) and centrifuged
822 at 14,000 rpm for 10 minutes. The supernatant was collected and protein concentration
823 was determined using Bradford reagent (BioRad). 10 µg protein was resolved on 4-12%
824 Bis-Tris gels (Life Technologies) and transferred to Immobilon-P nitrocellulose membrane
825 (Millipore) at 66V for 90 minutes. Subsequently, proteins were detected using anti-FASN

826 (1:2,000, Abcam ab128870) and anti- β -Actin (1:10,000, Abcam ab8226) antibodies and
827 proteins were visualized on X-ray film using Super Signal chemiluminescence reagent
828 (Thermo Scientific).

829

830 **Immunofluorescence**

831 Cells were seeded on cover slips and fixed with 4% paraformaldehyde in PBS for 10
832 minutes at room temperature. Cells were permeabilized with 1% NP-40 in antibody dilution
833 solution (PBS, 0.2% BSA, 0.02% sodium azide) for 10 minutes and blocked with 1% goat
834 serum for 45 minutes. Cells were incubated with anti-V5 (1:250, Abcam ab27671) and
835 anti-GOLGA2 antibodies (1:250, Sigma HPA021799) for 1 hour at room temperature.
836 Subsequently, cells were incubated with Alexa Fluor488 goat anti-mouse (1:500,
837 Invitrogen A-11001) or Alexa Fluor647 anti-rabbit antibodies (1:500, Invitrogen A-21245)
838 and counterstained with 1 μ g/ml DAPI (Cell Signaling Technology, 4083S) for 45 minutes
839 in the dark. Cells were visualized by confocal microscopy (Zeiss LSM 880).

840

841 **Protein expression analysis by flow cytometry**

842 Cells were detached using accutase (GIBCO), washed in PBS and 250k cells were stained
843 with PE-LDLR at 2 μ g/ml (1:100, BD Bioscience 565653) for 20 minutes at 4°C and
844 Zombie NIR (BioLegend 423105) cell viability solution at 25 ng/ml (1:2,000) for 5 minutes
845 at room temperature. Staining was measured using an LSR Fortessa flow cytometer (BD
846 Bioscience).

847

848 **RNA-sequencing**

849 Sample preparation: HAP1 WT, *FASN* KO and *C12orf49* KO cells were cultured in minimal
850 DMEM medium for 48h and either control treated or serum-starved for 4 hours as

851 indicated. Each cell line was cultured and processed in three biological replicates. RNA
852 was extracted using the RNeasy Kit (QIAGEN) according to manufacturer's instructions.
853 18 total RNA samples were DNase treated using RNase-free DNase Set (Qiagen, 79254).
854 Samples were submitted for mRNA-Seq at the Donnelly Sequencing Centre at the
855 University of Toronto (<http://ccbr.utoronto.ca/donnelly-sequencing-centre>). RNA was
856 quantified using Qubit RNA BR (Thermo Fisher Scientific, Q10211) fluorescent chemistry
857 and 1 ng was used to obtain RNA Integrity Number (RIN) using the Bioanalyzer RNA 6000
858 Pico kit (Agilent Technologies, 5067-1513). Lowest RIN was 9.5; median RIN score was
859 9.8. 1000 ng per sample was then processed using the NEBNext Ultra II Directional RNA
860 Library Prep Kit for Illumina (New England Biolabs, E7760L) and included polyA-
861 enrichment using NEBNext Poly(A) mRNA Magnetic Isolation Module (New England
862 Biolabs, E7490L), fragmentation for 15 minutes at 94°C prior to first strand synthesis, and
863 8 cycles of amplification after adapter ligation. 1µL top stock of each purified final library
864 was run on an Agilent Bioanalyzer dsDNA High Sensitivity chip (Agilent Technologies,
865 5067-4626). The libraries were quantified using the Quant-iT dsDNA high-sensitivity
866 (Thermo Fisher Scientific, Q33120) and were pooled at equimolar ratios after size-
867 adjustment. The final pool was run on an Agilent Bioanalyzer dsDNA High Sensitivity chip
868 and quantified using NEBNext Library Quant Kit for Illumina (New England Biolabs,
869 E7630L). The quantified pool was hybridized at a final concentration of 400 pM and
870 sequenced paired-end on the Illumina NovaSeq6000 platform using a S2 flowcell at 2x151
871 bp read lengths.

872

873 Data Processing: Samples were mixed to obtain an average of 35 million clusters that
874 passed filtering. Reads shorter than 36bp on either read1 or read2 were removed prior to
875 mapping. Reads were aligned to reference genome hg38 and Gencode V25 gene models
876 using the STAR short-read aligner (v2.6.0a) (REF). Approximately 80% of the filtered

877 reads mapped uniquely, and the read counts from each sample, computed by STAR, were
878 merged into a single matrix using R. The raw and processed data will be deposited in the
879 GEO database upon publication of manuscript.

880

881 Differential expression: Differentially expressed genes were identified using the
882 Bioconductor packages limma (v3.32.10) and edgeR (v3.24.3). The read count matrix was
883 filtered using the filterByExpr() function using default parameters. Principal Components
884 Analysis was performed to examine the main treatment effects, and to exclude the
885 presence of confounding batch effects, using the base R function prcomp(). Samples were
886 normalized using calcNormFactors(method="TMM") from edgeR and transformed to log₂
887 using voom(). Next, a design matrix was specified to fit coefficients for the CRISPR
888 knockouts, presence or absence of FBS, and an interaction term to examined differences
889 in the FBS effect in the mutant backgrounds. Differentially expressed genes were
890 extracted using topTable() with log₂(fold-change) > 0.58 and adjusted P-value less than
891 0.05.

892

893 **Quantitative real-time (qRT)-PCR analysis**

894 HAP1 WT, *FASN* KO and *C12orf49* KO cells were cultured in minimal DMEM medium for
895 48h and either control treated or serum-starved for 4 hours as indicated. RNA was
896 extracted using the RNeasy Kit (QIAGEN) according to manufacturer's instructions. RNA
897 was converted into cDNA using the cVilo master mix (ThermoScientific) according to
898 manufacturer's instructions. The cDNA was amplified and quantified by quantitative PCR
899 using the Maxima SYBR Green PCR master mix (ThermoScientific) according to
900 manufacturer's instructions. Transcript levels were normalized to *GAPDH* (see Table S8
901 for primer sequences).

902

903 **Metabolite profiling**

904 HAP1 WT and *FASN*-KO cells were cultured in minimal medium for 3 days. Cells were
905 washed twice in warm PBS and subsequently flash frozen on liquid nitrogen. Cells were
906 scraped in chilled extraction solvent (40% Acetonitrile: 40% Methanol: 20% water, all
907 HPLC grade), transferred to clean tubes and shaken for one hour at 4°C and subsequently
908 centrifuged at 4°C at max speed for 10 minutes. The supernatants were transferred to a
909 clean tube and dried in a speedvac then stored at -80°C until mass spec analysis. Samples
910 were reconstituted in water containing Internal Standards D7-Glucose and ¹³C₁₅N-
911 Tyrosine and injected twice through the HPLC (Dionex Corporation) for positive and
912 negative mode analysis using a reverse phase column (Inertsil ODS-3, 4.6 mm internal
913 diameter, 150 mm length, and 3 μM particle size). In positive mode analysis, the mobile
914 phase gradient ramped from 5% to 90% acetonitrile in 16 minutes, remained for 1 minute
915 at 90%, then returned to 5% acetonitrile in 0.1% acetic acid over two minutes. In negative
916 mode, the acetonitrile composition ramped from 5 to 90% in 10 minutes, remained for 1
917 minute at 90%, then returned to 5% acetonitrile in mobile phase (0.1% tributylamine,
918 0.03% acetic acid, 10% methanol). The total runtime in both the positive and negative
919 modes was 20 minutes, the samples were maintained at 4°C, and the injection volume
920 was 10 μL. An automated washing procedure was included before and after each sample
921 to avoid any sample carryover.

922

923 The eluted metabolites were analyzed at the optimum polarity in MRM mode on an
924 electrospray ionization (ESI) triple-quadrupole mass spectrometer (ABSciex 5500 Qtrap).
925 The mass spectrometric data acquisition time for each run was 20 minutes, and the dwell
926 time for each MRM channel was 10 ms. Mass spectrometric parameters were as
927 previously published (Abdel Rahman *et al.*, 2013). Metabolite peak areas were determined
928 using Multiquant software (SCIEX, Toronto, ON, Canada), normalized to internal standard

929 in each mode yielding an area ratio and then further normalized to total cell number for
930 each sample and Malonyl-CoA levels were further normalized to WT cells.

931

932 **QUANTIFICATION AND STATISTICAL ANALYSIS**

933 **Guide Mapping and Quantification**

934 FASTQ files from single read sequencing runs were first trimmed by locating constant
935 sequence anchors and extracting the 20 bp gRNA sequence preceding the anchor
936 sequence. Pre-processed paired reads were aligned to a FASTA file containing the TKOv3
937 library sequences using Bowtie (v0.12.8) allowing up to 2 mismatches and 1 exact
938 alignment (specific parameters: -v2 -m1 -p4 --sam-nohead). Successfully aligned reads
939 were counted, and merged along with annotations into a matrix.

940

941 **Scoring of quantitative genetic interactions: the qGI score**

942 To identify and quantify genetic interactions (GI), genome-wide CRISPR/Cas9 screens
943 were performed using the TKOv3 gRNA library in HAP1 coisogenic cell lines. Coisogenic
944 knockout (KO) “query” cell lines were obtained from Horizon Genomics (see above) or
945 generated by introducing mutations in target genes of interest (see above) in the parental
946 HAP1 cells, which we consider as wild-type (WT). The TKOv3 library contains 71,090
947 guide (g)RNAs that target ~18k human protein-coding genes, most of them with four
948 sequence-independent gRNAs (Hart *et al*, 2017). To quantify GIs, log₂ fold-changes (LFC)
949 between read-depth normalized gRNA abundance in the starting population (T0) and the
950 endpoint (T18) were computed. Matched T0 measurement assured that differences
951 between screens during library infection and Puromycin selection would not result in false
952 positive GIs. Matched T0 were stabilized using the median across many T0
953 measurements (common T0), and those two estimates were combined in a weighted
954 fashion to minimize correlation between GI scores and residual T0 (matched T0 – common

955 T0). gRNA-level residual scores were derived for a given genetic background by
956 estimating a non-interacting model between LFC values in this background and 21 WT
957 HAP1 backgrounds. To do so, for each WT-KO screen pair the population of LFC values
958 were M-A-transformed, which contrast the per-gRNA LFC difference M with per-gRNA
959 mean A. A Loess regression was fitted, which was additionally locally stabilized by binning
960 the data along A and considered equal bin sizes and equal numbers of data points in every
961 bin. For each gRNA, this resulted in 21 residual scores, which represent the contrasts of
962 a given KO with the 21 WT HAP1 screen. Under the assumption that genetic interactions
963 are sparse and that experimental artifacts such as batch effects would introduce additional
964 signal into the population of residual values, we computed a weighted mean of its 21
965 residual scores by giving a higher weight to WT HAP1 screens with lower absolute residual
966 mean of all 71k gRNAs. We refer to the resulting value for each gRNA as the “guide-level”
967 GI score. Those guide-level GI scores were further normalized. First, locally-defined shifts
968 towards negative or positive scores were identified and normalized, based on genome
969 location of the target genes. Next, to remove unwanted effects that would arise from
970 screen-to-screen variability, we quantified guide-level GI scores for each of the 21 WT
971 HAP1 screens by contrasting a given WT screen to the remaining WT screens (as
972 described for the KO-WT comparison above). Patterns that explain substantial variance
973 among these WT guide-level GI scores are likely to correspond with unwanted
974 experimental artefacts. To remove these artefacts from the GI data, we performed singular
975 value decomposition (SVD) on guide-level GI scores of the HAP1 WT screens only. We
976 then projected guide-level GI scores onto the left singular vectors, and subtracted the
977 resulting signal from the GI scores.

978

979 Finally, we computed gene-level genetic interaction scores. First, gRNAs were
980 excluded when their guide-level GI profile disagreed with those of the remaining gRNAs

981 against the same gene. Specifically, the mean within-gene guide-level GI profile Pearson
982 correlation coefficient was computed. For the gRNA with the lowest value we tested if (i)
983 the mean of all those four gRNA values for a given gene was above a selected threshold,
984 which indicated that sufficient signal was present in the guide-level GI profiles, and (ii) the
985 lowest value differed from this mean. All remaining guide-level GI values per gene were
986 mean-summarized and their significance was computed using limma's moderated t-test
987 followed by Benjamini-Hochberg multiple testing correction.

988

989 **Screen reproducibility analysis**

990 Reproducibility of the gRNA library screening data in FASN-KO cells was tested across
991 three independent screens. The three screens were started from independent infections
992 with lentivirus packaged gRNA library and performed as described above. To assess
993 reproducibility of fitness effects, a log₂ fold-change (LFC) quantifying the drop-out
994 between T0 (after puromycin selection) and T18 (endpoint) was computed for each gene
995 by mean-summarizing the respective four gRNA LFC values. The Pearson correlation
996 coefficients (PCCs) were computed between LFC values of all three pairs of independent
997 replicates.

998

999 Our experiments were designed to quantify fitness effect differences due to the
1000 introduction of a specific mutation into an otherwise isogenic background (i.e. GIs). To
1001 assess reproducibility of GIs, PCCs were computed between qGI values of all pairs of
1002 independent replicates.

1003

1004 To test reproducibility of genes, each gene's contribution to the covariance
1005 between a pair of FASN-KO screens was computed and divided by the product of standard

1006 deviations of both given screens. The resulting three pairwise (for replicates A-B, A-C, B-
1007 C) gene-level scores were mean-summarized to a FASN qGI reproducibility score.

1008

1009 **Reproducibility analysis of FASN interactions**

1010 We used an MCMC-based approach to measure the reproducibility of *FASN* GIs.

1011 Specifically, we first independently scored the three independent *FASN* replicate screens

1012 and applied an FDR threshold of FDR 50% to generate positive and negative GI profiles

1013 for each of the three screens. MCMC was then used to jointly infer false negative and false

1014 positive rates, as well as a binary consensus *FASN* GI profile (separately for

1015 positive/negative GI). Then, using this consensus profile as a standard for evaluation

1016 (assuming pairs with posterior probability of interaction of > 0.5 as positives), we measured

1017 precision and recall statistics (averaged across the three screens) at two different cut-offs:

1018 a “standard” cut-off (absolute qGI score > 0.5 and FDR 50%) and a “stringent” cut-off

1019 (absolute qGI score > 0.7 and FDR 20%).

1020

1021 **Precision-recall analysis**

1022 To control quality of genome-wide gRNA screens, gene-level fitness effects were

1023 estimated by computing a log₂ fold-change (LFC) quantifying the drop-out between T₀

1024 (after puromycin selection) and T₁₈ (endpoint) for each gene and mean-summarizing the

1025 respective four gRNA LFC values. Gold-standard essential (reference) and non-essential

1026 (background) gene sets were taken from Hart et al., 2015(Hart *et al*, 2015) and Hart et al.,

1027 2017(Hart *et al*, 2017). For the identification of reference genes using LFC values of a

1028 given screen was assessed by computing precision over true positive statistics.

1029

1030 **Functional evaluation of genetic interactions**

1031 To calculate the enrichment of metabolic GIs in different functional standards, we
1032 separated the metabolic GIs in two different sets: all (background) GI scores and high
1033 confidence (reference) GI (FDR < 0.5, |qGI| >= 0.5). Then we calculated the fold
1034 enrichment of the reference set against the background set in a particular functional
1035 standard. First, we computed the overlap of metabolic GI pairs as co-annotations in the
1036 standard. Then we divided the overlap density of the background set into the overlap
1037 density of the reference set to determine the fold enrichment. Once we got the fold
1038 enrichments, we calculated p-values on the actual overlap counts of the reference and
1039 background sets according to hypergeometric tests. We used four different functional
1040 standards: Human functional network (Greene *et al*, 2015), GO biological processes
1041 (Ashburner *et al*, 2000), Pathway (Canonical pathways from (Liberzon *et al*, 2011)), and
1042 HumanCyc (Romero *et al*, 2005).

1043

1044 **Gene ontology enrichment analysis**

1045 Gene ontology (GO) enrichment analysis for the *FASN* and *C12orf49* GI screen and the
1046 BioID experiments were performed using the gProfileR R package using the GO-
1047 Bioprocesses, GO-Molecular Function and Reactome pathway standards. For the GI
1048 screens, enrichment analysis was performed for significant negative GIs (qGI < -0.5, FDR
1049 < 0.5), enriched pathways (p<0.05, maximum term size 100) with a similarity of > 50%
1050 were collapsed using the Cytoscape Enrichment Map function and the mean percentage
1051 overlap of hits within the term were visualized on a bar plot. For the BioID experiments,
1052 enrichment analysis was performed for significant hits (spectral counts > 10, FDR < 0.01),
1053 enriched pathways (p<0.05) with a similarity of > 50% were collapsed using the Cytoscape
1054 Enrichment Map function and the mean percentage overlap of hits within the term were
1055 visualized on a bar plot.

1056

1057 **Statistical Analysis**

1058 For all experiments the number of technical and/or biological replicates are listed in the
1059 figure legends or text. Unless otherwise indicated, statistical significance was assessed
1060 via one or two factor ANOVA with Fisher's Least Significant Difference test. Statistical
1061 analyses were performed using GraphPad Prism 8 (GraphPad Software, La Jolla,
1062 California, USA) or the R language programming environment.

1063

1064 **DATA AND CODE AVAILABILITY**

1065 The datasets generated and analysed in this study are included in the manuscript. The
1066 raw fastq files for all of the sequencing data are available upon request and will be
1067 uploaded to GEO upon publication. Descriptions of the analyses, tools and algorithms are
1068 provided in the methods section of this article. Custom code for generating gRNA counts
1069 from fastq files and code for generating qGI-scores will be made available on Github upon
1070 publication.

1071 **FIGURE LEGENDS**

1072 **Figure 1. Genome-scale identification of digenic interactions with *FASN*.**

1073 (a) Schematic outline for the identification of genetic interactions in coisogenic HAP1 cell
1074 lines. *FASN* knockout (KO) and wildtype parental cells are infected with a lentiviral
1075 genome-wide CRISPR gene KO library (TKOv3) and gRNA abundance is determined
1076 using Illumina sequencing of guide RNA (gRNA) sequences amplified from extracted
1077 genomic DNA from the starting cell population (T0) and end time point (day 18, T18) of
1078 the screen.

1079 (b) Schematic outline for scoring quantitative genetic interactions (qGI) across coisogenic
1080 query cell lines. First, the \log_2 fold-change (LFC) for each gRNA comparing sequence
1081 abundance at the starting (T0) and end time point (T18) in a given query KO or wildtype
1082 (WT) cell population are computed. Differential LFC for each gRNA are then estimated by
1083 comparing its LFC in WT and query KO cells. A series of normalization steps and statistical
1084 tests are applied to these data to generate gene-level qGI scores and false discovery rates
1085 (see Methods for details). The LFC scatterplot (bottom left graph) visualizes differential
1086 fitness defects in a specific query KO and WT cells, whereas the volcano plot (bottom right
1087 graph) visualizes qGI scores for a specific query.

1088 (c) Replicate analysis of gene loss of function fitness phenotypes in *FASN* screens.
1089 Scatter plots of LFC associated with perturbation of 17,804 individual genes derived from
1090 a *FASN* query KO mutant screen conducted in triplicate. Reproducibility of fitness effects
1091 were determined by measuring Pearson correlation coefficients (r) between all possible
1092 pairwise combinations of *FASN*-KO replicate screens.

1093 (d) Evaluation of *FASN* quantitative genetic interactions (qGIs). qGI scores were
1094 measured by comparing the LFC for every gene represented in the TKOv3 gRNA library
1095 in a *FASN*-KO with those observed in a WT cell line, as described. Scatter plots show
1096 *FASN* genetic interactions (qGI scores) derived from all possible pairwise combinations of

1097 three biological replicate screens. The Pearson correlation coefficient (r), based on
1098 comparison of all qGI scores (r shown in grey, calculated on all the grey, blue and purple
1099 data points in the scatter plots), or only genetic interactions that exceed a given
1100 significance threshold ($|qGI| > 0.5$, $FDR < 0.5$) in one (blue) or two screens (purple).

1101 **(e)** Validation of *FASN* negative genetic interaction. Bar plots depict the ratio of WT and
1102 *FASN*-KO (2 independent clones, c1 and c2) cells carrying a gRNA targeting *SLCO4A1*,
1103 *LDLR* or *C12orf49*, which all showed a negative interaction with *FASN*, compared to a
1104 gRNA targeting *AAVS1* (intergenic control). Experiments were performed with three
1105 independent gRNAs targeting each genetic interaction screen hit. All data are represented
1106 as means \pm standard deviation ($n = 3$ or 4), $**p < 0.01$, and $*p < 0.05$; one-way ANOVA.

1107 **(f)** *FASN* negative and positive genetic interactions. A scatter plot illustrating the fitness
1108 (LFC) of 450 genes individually targeted in a *FASN*-KO vs. WT parental HAP1 cell line.
1109 Each of the 450 genes shown exhibited a significant genetic interaction in at least 2 out of
1110 3 *FASN*-KO replicate screens ($|qGI| > 0.5$, $FDR < 0.5$). Negative (blue) and positive
1111 (yellow) *FASN* genetic interactions are shown. Node size corresponds to the mean
1112 absolute qGI score derived from 3 replicate screens. Genes with mean absolute qGI score
1113 > 1.5 as well as selected negative interactions involving genes with established roles in
1114 lipid metabolism are indicated. [Inset] Scatter plot of *FASN* genetic interaction scores for
1115 all 17,804 genes targeted by the TKOv3 gRNA library where the color indicates density of
1116 genes.

1117 **(g)** Enrichment for Gene Ontology (GO) molecular function, GO bioprocesses and
1118 Reactome terms among genes that exhibited a significant negative genetic interaction with
1119 *FASN* (significant in at least two *FASN* replicates, $|qGI| > 0.5$, $FDR < 0.5$). The number of
1120 genes annotated to each term and shown to interact with *FASN* are indicated.

1121 (h) Schematic depicting the function of selected *FASN* negative interactions known to be
1122 involved in lipid uptake and homeostasis pathways (red), vesicle transport (black) and
1123 glycosylation (blue).

1124

1125 **Figure 2. Querying five additional lipid metabolism genes for digenic interactions.**

1126 (a) Schematic diagram showing key steps in fatty acid metabolism. The genes encoding
1127 the proteins mediating these key steps, which are also query genes for genetic interaction
1128 screens described in the main text, are labelled in red.

1129 (b-f) Volcano plots showing qGI scores versus false discovery rates ($-\log_{10}$ p-value) for
1130 the results of the (b) *LDLR*-KO, (c) *SREBF2*-KO, (d) *ACACA*-KO, (e) *SREBF1*-KO and (f)
1131 *C12orf49*-KO screens. Colored dots indicate genes that meet the standard threshold of
1132 $|qGI| > 0.5$, $FDR < 0.5$, where positive GIs are indicated in yellow and negative GIs in blue.
1133 The dot size is proportional to both qGI and FDR, calculated as described in the methods.
1134 Genes with $|qGI|$ scores > 1.5 as well as selected top negative GI hits associated with lipid
1135 metabolism, citrate synthesis and transport are indicated.

1136

1137 **Figure 3. Genetic interactions reveal multiple levels of functional enrichment.**

1138 (a) Dot plot of normalized pathway enrichment scores on the HumanCyc category level,
1139 calculated from qGIs across all six query genes (*FASN*, *C12orf49*, *LDLR*, *SREBF2*,
1140 *ACACA*, *SREBF1*). A GI is identified for a query-library pair if the $|qGI| > 0.5$ and $FDR <$
1141 0.5 . Enrichment for positive (yellow) and negative (blue) GIs is tested in each of the 10
1142 HumanCyc main pathway categories using a hypergeometric test. Enrichment with p-
1143 value < 0.05 are blue (negative GI) and yellow (positive GI). Dot size is proportional to the
1144 fold-enrichment in the indicated categories and specified in the legend. Categories
1145 indicated in bold are further expanded in part (b) and in Supplemental Figure 3a.

1146 **(b)** Dot plot of normalized pathway enrichment of GIs on a sub-category level, calculated
1147 as described in part (a), except that sub-categories were examined inside the Biosynthesis
1148 and Macromolecule Modification HumanCyc branches. Enrichment with p-value < 0.05
1149 are blue (negative GI) and yellow (positive GI). Dot size is proportional to the fold-
1150 enrichment in the indicated categories and specified in the legend. Categories indicated
1151 in bold text are further expanded in part (c).

1152 **(c)** Matrix dot plot of pathway enrichments of GIs for the fatty acid and lipid biosynthesis
1153 and protein modification sub-categories. Dots show positive (yellow) or negative (blue) z-
1154 transformed qGI scores summarized at a pathway-level. qGI scores were first z-score
1155 transformed at a gene-level for each genome-wide query screen separately. Then, a mean
1156 z-score was calculated for each pathway for a given query screen. Dot size corresponds
1157 to the absolute z-transformed mean qGI score, grey dots represent $|z| < 0.5$. Pathways
1158 marked with an asterisk are annotated to both protein modification and carbohydrate
1159 biosynthesis pathways. Bold pathways are shown in (d-e). Pathways were displayed if
1160 they shared an absolute z-score larger than 1.5 with any query gene.

1161 **(d-f)** Gene-level heatmaps for genes involved in enriched pathways. qGI scores between
1162 query genes and all genes from the selected pathways. Positive and negative qGI scores
1163 are indicated in yellow and blue, respectively.

1164

1165 **Figure 4. *C12orf49* genetic interaction profile suggests a functional role in lipid**
1166 **metabolism.**

1167 **(a)** Bar plot depicting pathway enrichment of negative genetic interactions with *C12orf49*
1168 ($|qGI| > 0.5$, FDR < 0.5) using GO molecular functions, GO bioprocesses and Reactome
1169 standards. Significantly enriched gene sets ($p < 0.05$, maximum term size 100). Bars
1170 depict mean percentage overlap with the indicated term, and the numbers on each bar

1171 indicate the number of genes overlapping a particular term and term size, respectively.

1172 The greyscale color legend for p-values is indicated on the right.

1173 (b) Scatter plot of *C12orf49* and *FASN* qGIs depicting GI overlap between *C12orf49* and

1174 *FASN* qGI scores. *FASN* qGI scores are represented as the mean between three

1175 independent screens. A common negative GI is called if it is significant (qGI < -0.5, FDR

1176 < 0.5) in the *C12orf49*-KO screen and significant in 2 of 3 *FASN*-KO screens (indicated in

1177 blue). The top 10 strongest common GIs, lipid metabolism and vesicle trafficking genes

1178 are labelled.

1179 (c) Scatter plot of *C12orf49* and *LDLR* qGIs depicting GI overlap between *C12orf49* and

1180 *LDLR* qGI scores. A common negative GI is called if it is significant (qGI < -0.5, FDR <

1181 0.5) in both screens (indicated in blue). The top 10 strongest common GIs and lipid

1182 metabolism genes are labelled.

1183 (d) Bar plot indicating the *C12orf49* profile similarity across genome-wide DepMap

1184 CRISPR/Cas9 screens. Similarity (i.e. co-essentiality) was quantified by taking all pairwise

1185 gene-gene Pearson correlation coefficients of CERES score profiles across 563 screens

1186 (19Q2 DepMap data release). The top 18 out of 17,633 gene profiles most similar to

1187 *C12orf49* are shown. Genes associated with lipid metabolism are indicated in black.

1188 (e) Volcano plot of pathway enrichment for *C12orf49* co-essential genes. *C12orf49* co-

1189 essentiality profile scores for all 17,634 genes represented in the DepMap were mean-

1190 summarized by pathway as defined in the HumanCyc standard (Romero *et al.*, 2004).

1191 Tendencies towards pathway-level similarity (co-essentiality) and dissimilarity (exclusivity)

1192 with *C12orf49* were tested using a two-sided Wilcoxon rank-sum test followed by multiple

1193 hypothesis correction with the Benjamini and Hochberg procedure.

1194

1195 **Figure 5. *C12orf49* shuttles between ER and Golgi and regulates lipid uptake.**

1196 **(a)** Schematic outlining proximal protein capture using BioID mass spectrometry analysis
1197 (upper panel) and analysis of subcellular localization of C12orf49 BioID preys (lower
1198 panel). Barplots depicting the fraction of proteins localizing to indicated cellular
1199 compartments for preys captured with N-terminal (grey) or C-terminal (black) BirA*-tagged
1200 C12orf49 in 293 cells. The inset shows a schematic representation of the predicted
1201 topology and orientation of C12orf49 with respect to the cytoplasm and ER.

1202 **(b)** Pathway enrichment analysis of BioID preys captured with N-terminal (top panel) or C-
1203 terminal (bottom panel) BirA*-tagged C12orf49 using the GO molecular function, biological
1204 process and Reactome standards. Terms for significantly enriched gene sets ($p < 0.05$,
1205 maximum term size 100) are indicated and bars depict mean percentage overlap with the
1206 indicated term. Numbers indicate the number of genes overlapping a particular term and
1207 term size, respectively. The greyscale color legend for p-values is indicated on the right.

1208 **(c)** Immunofluorescence microscopy analysis of C-terminal V5-tagged C12orf49 in HAP1
1209 cells under normal (left) or serum-starved (right) growth condition. C12orf49-V5
1210 localization is shown in green, GOLGA2 is a marker of the Golgi apparatus and shown in
1211 red, and DAPI (blue) marks the nuclei. Scale bars correspond to 10 μm .

1212 **(d)** Bar plots showing the results of low density lipoprotein (LDL) uptake assays in the
1213 indicated cells using the Dil-LDL probe. All data are represented as means \pm standard
1214 deviation ($n = 2-6$). *** $p < 0.001$ and * $p < 0.05$; one-way ANOVA.

1215 **(e)** Bar plots indicating FPKM expression values from RNA sequencing data for *LDLR* and
1216 *LDLRAP1* in WT, *C12orf49*-KO, and *SREBF2*-KO cells under normal (+FBS) and serum-
1217 starved (-FBS) growth conditions as assessed by RNA sequencing ($n=3$).

1218 **(f)** Model summarizing functions and locations of key players in lipid metabolism, including
1219 LUR1 (C12orf49).

1220

1221 **SUPPLEMENTAL FIGURE LEGENDS**

1222 **Figure S1. Validation of *FASN*-KO cells and genetic interactions screens.**

1223 (a) Western blot depicting *FASN* and β -Actin levels in HAP1 parental wildtype (WT) and
1224 *FASN*-KO cells.

1225 (b) Bar plot depicting malonyl-CoA levels in HAP1 WT and *FASN*-KO cells as detected by
1226 mass spectrometry-based metabolite profiling, normalized to parent HAP1 WT cells (n=4);
1227 $p = 0.03$, Mann Whitney U test.

1228 (c) Growth curves of HAP1 WT cells depicting relative cell numbers over 3 days, plotted
1229 as a function of glucose concentration in mM, in either 0.5 mM (blue), 1 mM (red), 1.5 mM
1230 (yellow), or 2 mM (black) glutamine.

1231 (d) Histogram showing a frequency distribution of all pairwise Pearson correlation
1232 coefficients for LFC values (T0/T18) of the 21 WT HAP1 screens.

1233 (e) Precision-recall curves for the three CRISPR replicate screens in HAP1 *FASN*-KO cells
1234 using the reference core essential gene set (CEG2) defined in Hart *et al.*, 2017.

1235 (f) Fitness effect (log₂ fold-change, LFC) distributions for reference core essential (CEG2)
1236 and non-essential gene sets defined in Hart *et al.*, 2017 across the three *FASN*-KO query
1237 screens.

1238 (g) Scatter plot showing reproducibility scores as a function of qGI scores for a single
1239 *FASN*-KO screen (replicate A). Pairwise reproducibility of a qGI score was calculated by
1240 computing each gene's contribution to the covariance between a pair of screens divided
1241 by the sum of standard deviations. The reproducibility score represents the sum of those
1242 values across the three pairwise comparisons. Five genes with highest reproducibility
1243 scores and the most negative qGI scores with the *FASN*-KO screen (replicate A) are
1244 labelled.

1245 (h) Establishing the *AAVS1* target locus as a good negative control site in HAP1 WT and
1246 *FASN*-KO cells. Schematic depicting co-culture validation assays (upper panel). Parental

1247 WT and *FASN*-KO cells were stably transduced with color-coded gRNA expression
1248 vectors carrying an intergenic control or screen hit-targeting gRNA. Color-coded cells are
1249 mixed at an equal ratio, cultured over two weeks and the relative proportion of green and
1250 red cells was quantified by flow cytometry. Control co-culture experiments performed in
1251 parallel to the validation of hit genes depicted in main Figure 1e as indicated above each
1252 barplot (lower panel). Bar plots are depicting the color ratio of cells carrying two colour-
1253 coded gRNAs targeting *AAVS1* (intergenic control) across WT and two *FASN*-KO clones
1254 as indicated. Experiments were performed with three independent gRNA targeting *AAVS1*
1255 and using both color orientations. All data are represented as means \pm standard deviation
1256 ($n = 3$ or 4).

1257 (i) Scatter plots reproducibility scores as a function of qGI scores for the negative genetic
1258 interaction hits depicted in Figure 1h functioning in lipid uptake and homeostasis (red),
1259 vesicle transport genes (black) and glycosylation (blue).

1260 (j) Precision and recall values for GIs with *FASN* measured at the standard ($|qGI| > 0.5$,
1261 $FDR < 0.5$) and stringent ($|qGI| > 0.7$, $FDR < 0.2$) thresholds. Precision and recall values
1262 were computed using an MCMC-based approach (see Methods).

1263

1264 **Figure S2. Quality control of genetic interaction screens for fatty acid synthesis-**
1265 **related query genes.**

1266 (a) Precision-recall curves distinguishing the reference core essential gene set (CEG2)
1267 defined in Hart *et al.*, 2017 and a non-essential gene set in CRISPR screens in five HAP1
1268 knockout query cell lines (*LDLR*, *C12orf49*, *SREBF2*, *ACACA*, *SREBF1*-KO).

1269 (b) Fitness effect (LFC) distributions for reference core essential (CEG2) and non-
1270 essential gene sets defined in Hart *et al.*, 2017 across CRISPR screens in five HAP1 KO
1271 cell lines (*LDLR*, *C12orf49*, *SREBF2*, *ACACA*, *SREBF1*).

1272 (c) Bar plot of enrichment of co-annotation as defined by the Human Functional Network,
1273 Gene Ontology Bioprocesses (BP), HumanCyc or and aggregation of pathway standards
1274 (including REACTOME, KEGG or BIOCARTA) for genetic interactions identified across all
1275 six query genome-wide screens (*FASN*, *LDLR*, *C12orf49*, *SREBF2*, *ACACA*, *SREBF1*).
1276 See methods for details of analysis.

1277

1278 **Figure S3. Pathway enrichment analysis of genetic interactions for fatty acid**
1279 **synthesis-related query genes in additional HumanCyc sub-categories.**

1280 (a) Dot plot of normalized pathway enrichment values for aggregate GIs across the six
1281 query genes (*FASN*, *C12orf49*, *LDLR*, *SREBF2*, *ACACA*, *SREBF1*) with sub-categories
1282 from HumanCyc are indicated. A GI is identified for a query-library pair if the $|qGI| > 0.5$
1283 and $FDR < 0.5$. Enrichment for positive (yellow) and negative (blue) GI is tested inside
1284 Glycan Pathways and Generation of precursor metabolite and energy HumanCyc
1285 branches using a hypergeometric test. Enrichment with $p\text{-value} < 0.05$ are blue (negative
1286 GI) and yellow (positive GI). Dot size is proportional to the fold-enrichment in the indicated
1287 categories and specified in the legend.

1288

1289 **Figure S4. Overview of C12orf49, cancer associations, and functional correlates.**

1290 (a) Cartoon of C12orf49 protein sequence features and domains.

1291 (b-e) Kaplan Meier survival plots displaying univariate analysis of TCGA data across
1292 multiple tumor types including kidney, breast, liver and sarcoma for *C12orf49* high vs. low
1293 expressing tumor tissue (www.kmplot.com) (Nagy *et al*, 2018).

1294 (f-h) GI overlap between *C12orf49* and *SREBF2*, *SREBF1* and *ACACA* qGI scores shown
1295 as pairwise scatter plots with *C12orf49* as function of *SREBF2* (f), *SREBF1* (g) and
1296 *ACACA* (h). A common negative GI is called if it is significant ($qGI < -0.5$, $FDR < 0.5$) in

1297 both screens (indicated in blue). The top 10 strongest common GIs and lipid metabolism
1298 genes are labelled.

1299 (i) Profile similarity of *C12orf49* across genome-wide DepMap CRISPR/Cas9 screens.
1300 Similarity was quantified by taking all pairwise gene-gene Pearson correlation coefficients
1301 of CERES score profiles across 563 screens (19Q2 DepMap data release). The
1302 distribution of 17,633 CERES profile similarity is plotted as a quantile-quantile plot, and
1303 the top 18 most similar out of 17,633 genes are labelled. Genes associated with lipid
1304 metabolism are indicated in red.

1305 (j) Pathway analysis of *C12orf49* profile similarity. *C12orf49* profile similarity scores for all
1306 17,634 genes represented in the DepMap were mean-summarized by pathway as defined
1307 in the HumanCyc standard (Romero *et al.*, 2004). Tendencies towards pathway-level
1308 similarity (co-essentiality) and dissimilarity (exclusivity) with *C12orf49* were tested using a
1309 two-sided Wilcoxon rank-sum test with multiple hypothesis correction using the Benjamini
1310 and Hochberg procedure.

1311

1312 **Figure S5. Regulation of LDL uptake and LDLR expression by *C12orf49*.**

1313 (a) Bar plots showing the results of a low density lipoprotein (LDL) uptake assay across
1314 the indicated HAP1 cell lines using pHrodo-LDL probe. All data are represented as means
1315 \pm standard deviation ($n = 2-3$), *** $p < 0.001$, one-way ANOVA.

1316 (b) Bar plots showing the results of a transferrin uptake assay across the indicated HAP1
1317 cell lines using pHrodo-Transferrin probe. All data are represented as means \pm standard
1318 deviation ($n = 2-3$). *** $p < 0.001$, ** $p < 0.01$, and * $p < 0.05$; one-way ANOVA.

1319 (c) Gene ontology enrichment analysis of genes upregulated under serum starvation in
1320 HAP1 wildtype (WT), *C12orf49* or *SREBF2*-KO cells using GO molecular functions, GO
1321 bioprocesses and Reactome standards. Gene sets with overlapping members have been

1322 merged and bars depict mean percentage overlap with the indicated term. Numbers
1323 indicate the mean overlap and term sizes respectively.

1324 **(d)** Boxplots depicting mean expression and induction of genes assigned with the
1325 indicated term across HAP1 WT, *C12orf49* and *SREBF2*-KO cells under normal (+FBS)
1326 and serum-starved (-FBS) conditions (n=3), **p < 0.01, student's t test.

1327 **(e)** Bar plot of relative mRNA expression of LDLR across HAP1 WT, *FASN*-KO and
1328 *C12orf49*-KO cells (n=3). ***p < 0.001, one-way ANOVA.

1329 **(f)** Bar plot of LDLR surface expression across HAP1 wildtype (WT) and the indicated
1330 KO and rescue cell lines under normal (+FBS) or serum-starved (-FBS) conditions as
1331 assessed by flow cytometry. ***p < 0.001, two-way ANOVA.

1332 **SUPPLEMENTAL TABLES**

1333 Table S1 FASN qGI reproducibility analysis across *FASN* replicate screens.

1334 Table S2 Genetic Interaction Scores.

1335 Table S3 Pathway Enrichment Negative Genetic Interactions *FASN*, *C12orf49*

1336 Table S4 Pathway enrichment Genetic interactions z-scores.

1337 Table S5 BioID C12orf49.

1338 Table S6 Pathway enrichment BioID C12orf49.

1339 Table S7 RNAseq HAP1 WT, *C12orf49*-KO, *SREBF2*-KO plus-minus FBS.

1340 Table S8 Primer and Oligo List.

Figure 1

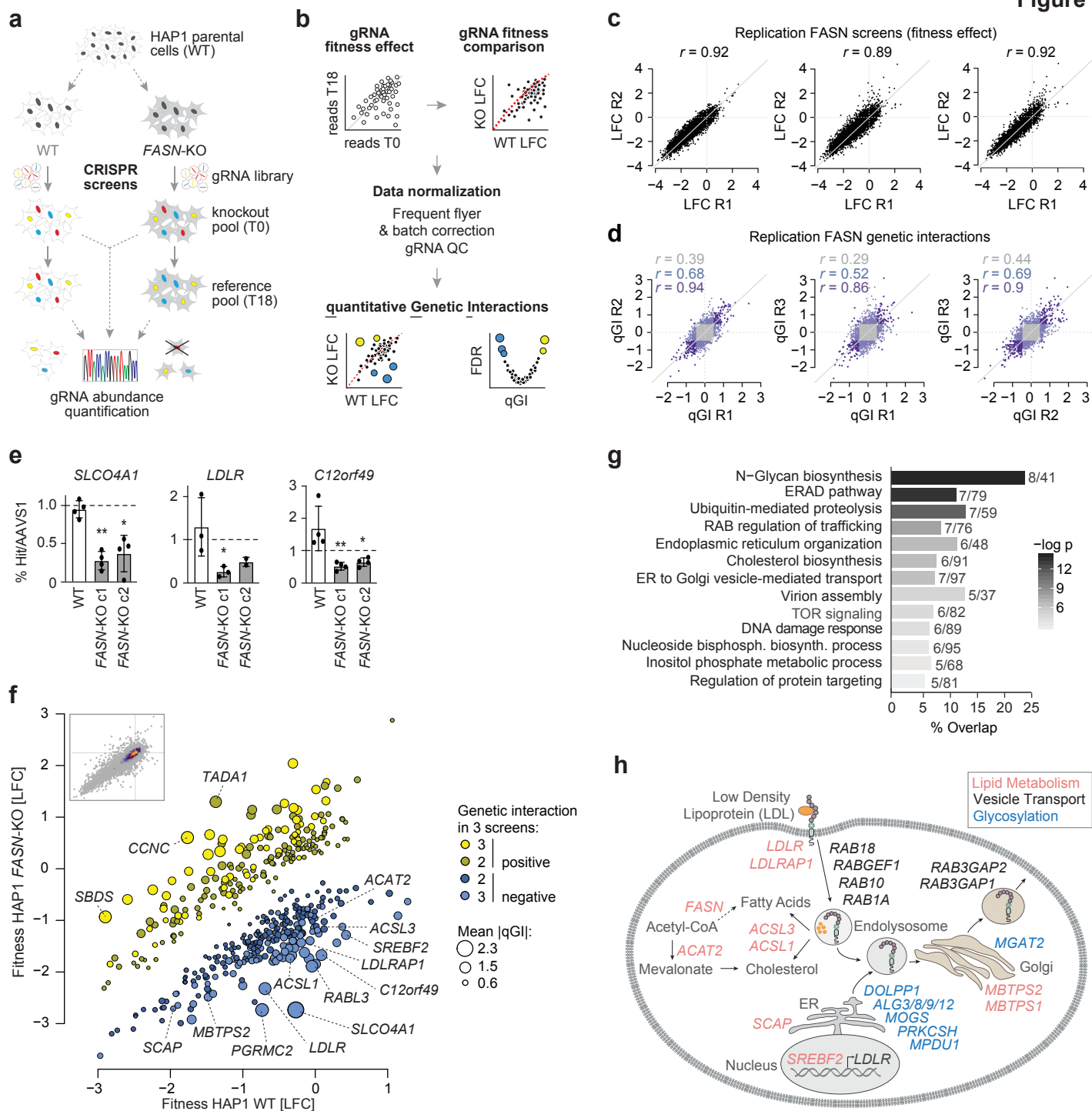


Figure 2

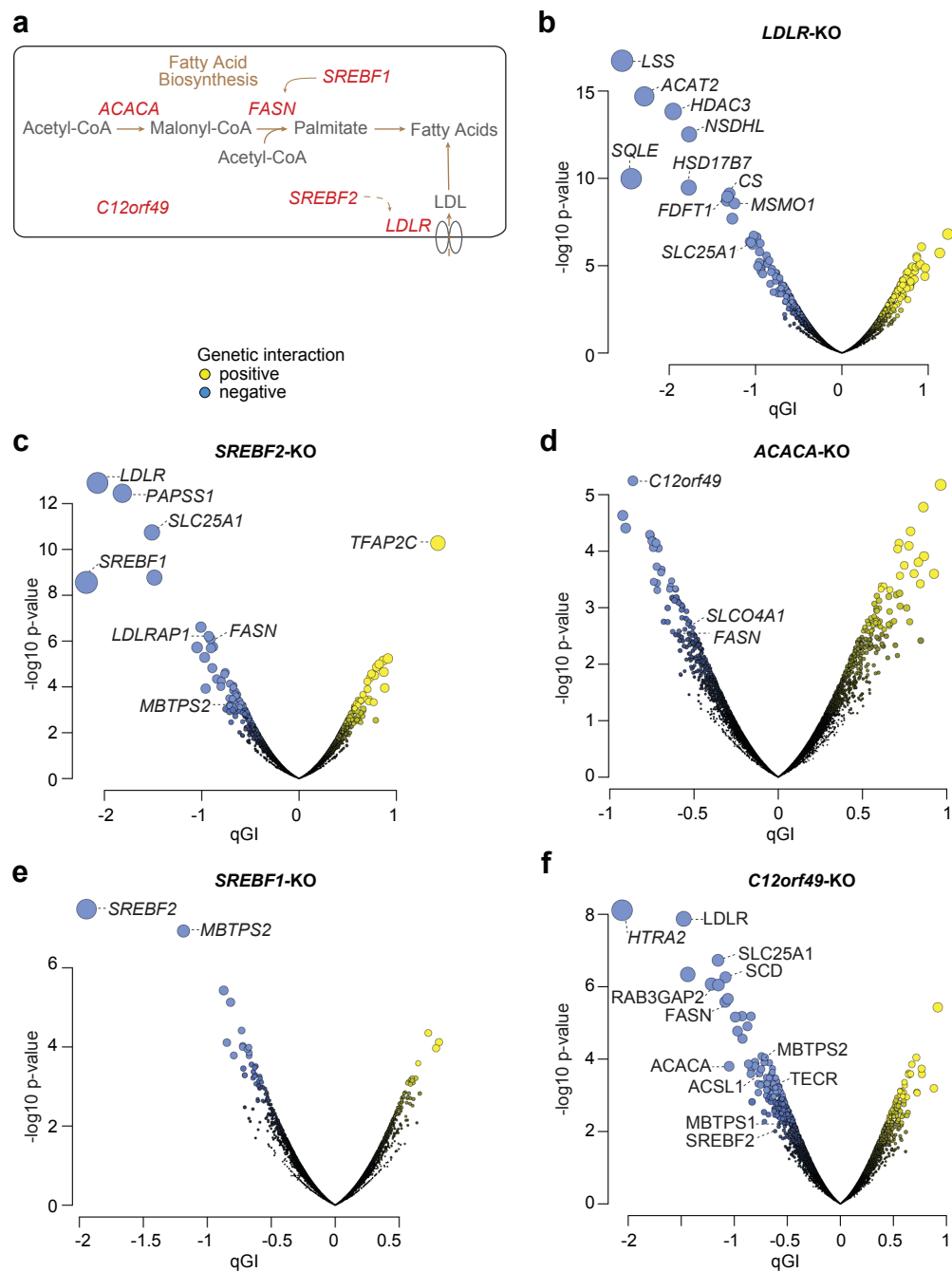
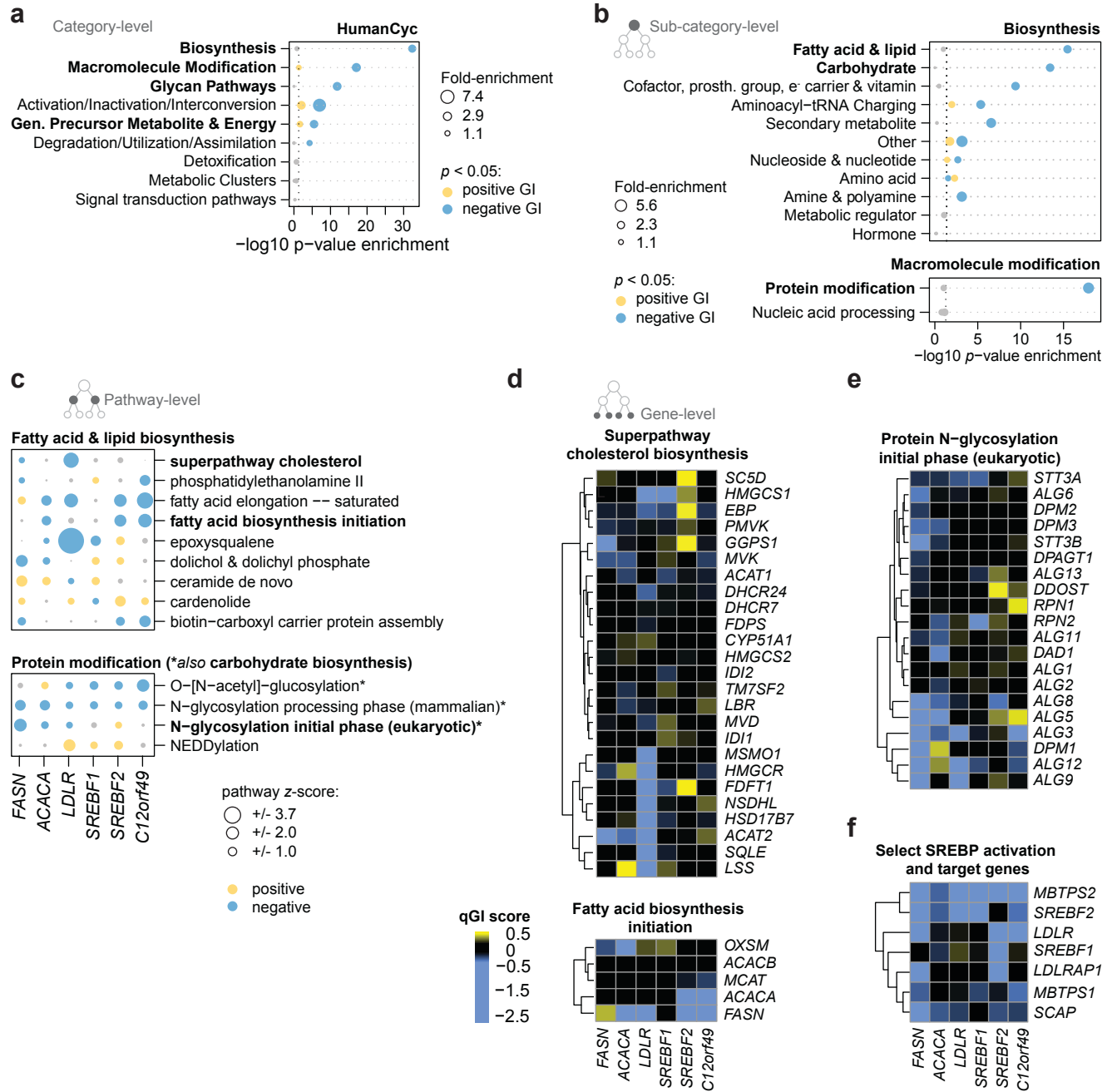


Figure 3



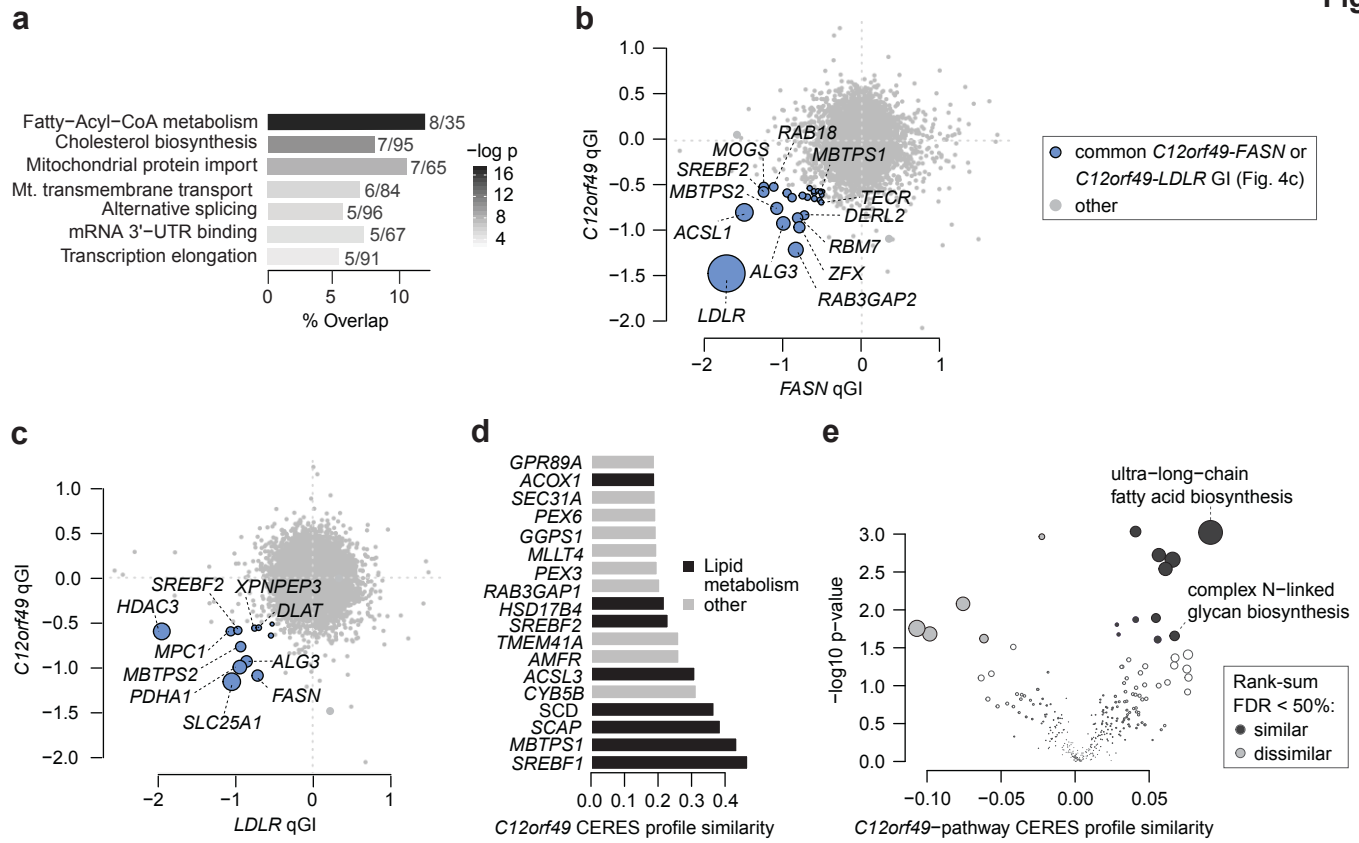
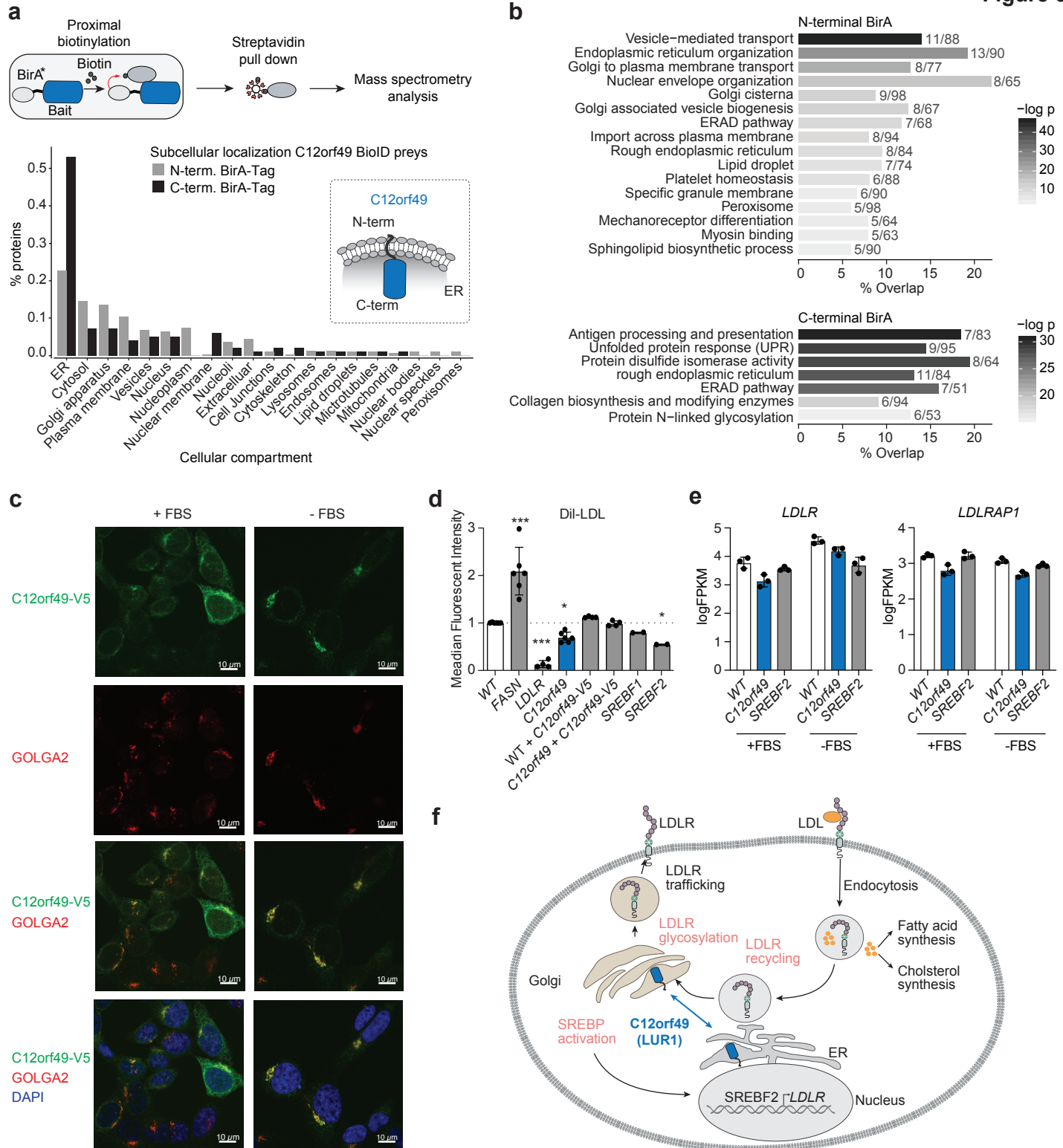


Figure 5



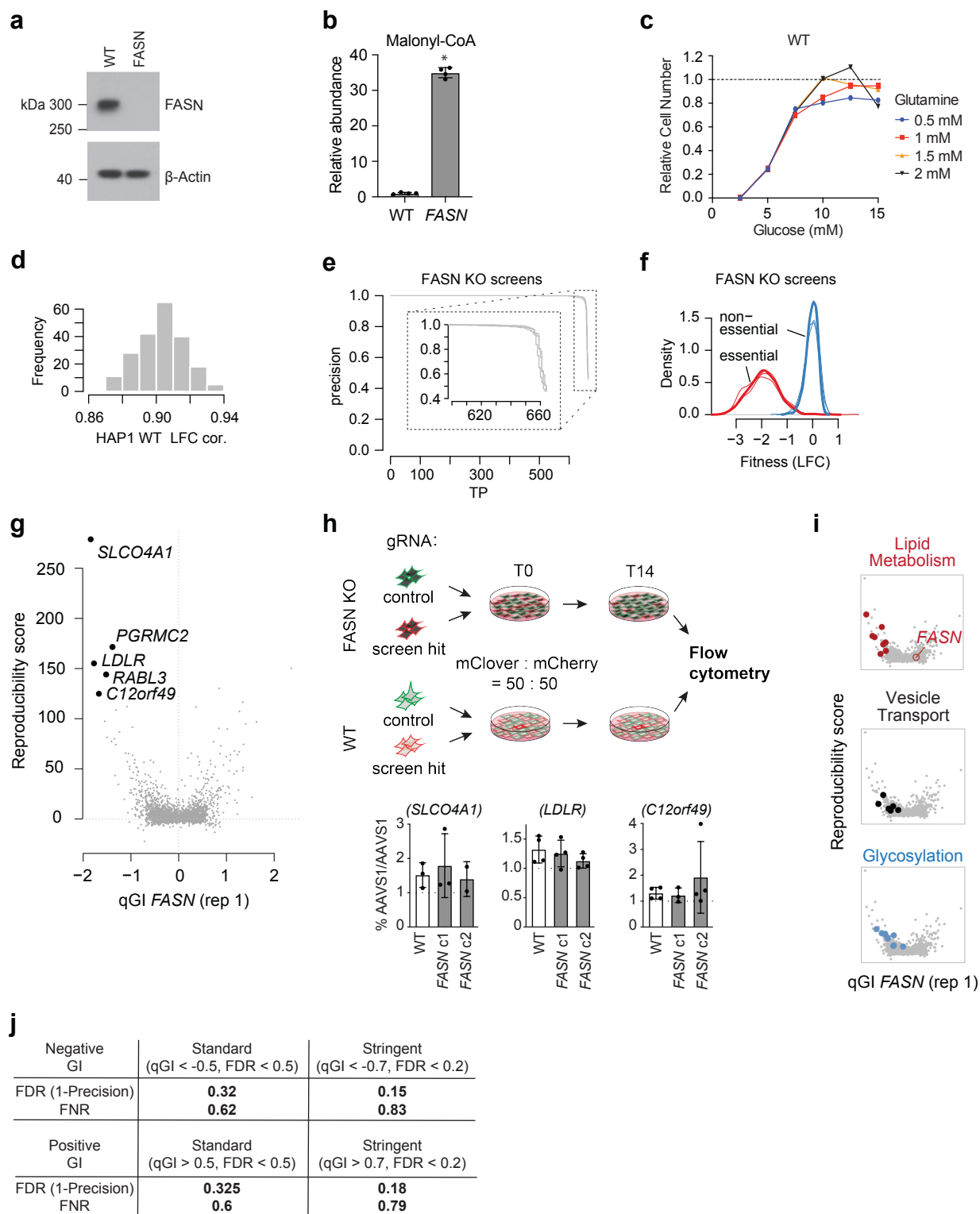
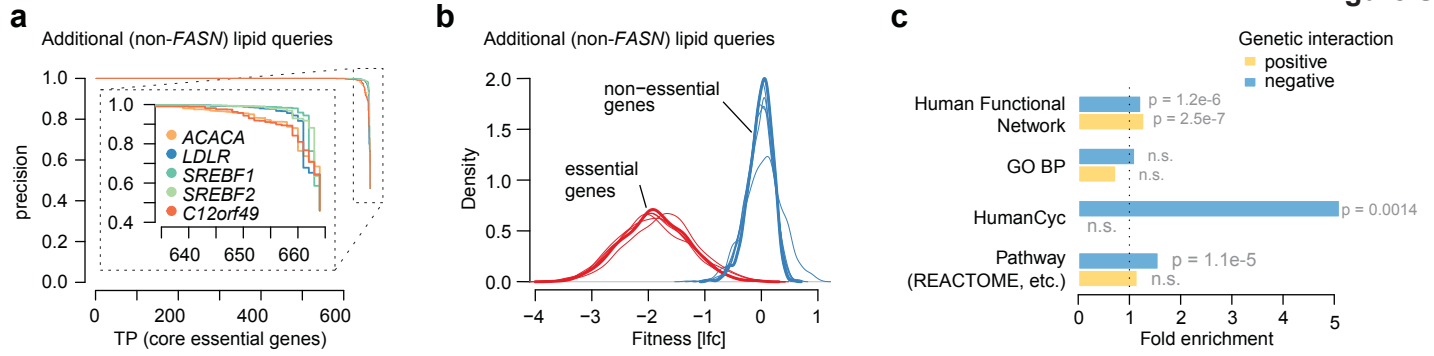


Figure S2



a

